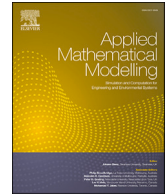


Contents lists available at [ScienceDirect](https://www.sciencedirect.com)

Applied Mathematical Modelling

journal homepage: www.elsevier.com/locate/apm

A multiphysics model for fluid-structure-electrophysiology interaction in rowing propulsion

Alessandro Nitti ^{a,*}, Michele Torre ^b, Alessandro Reali ^c, Josef Kiendl ^c,
Marco D. de Tullio ^a

^a Department of Mechanics, Mathematics and Management, Polytechnic University of Bari, Via Re David 200, Bari, 70125, Italy

^b Department of Civil Engineering and Architecture, University of Pavia, Via Ferrata 3, Pavia, 27100, Italy

^c Institute of Mechanics and Structural Analysis, Bundeswehr University, Werner-Heisenberg-Weg 39, Neubiberg, 85577, Germany

ARTICLE INFO

Keywords:

Jellyfish
Immersed boundary
Isogeometric analysis
Active strain
Finite differences

ABSTRACT

Jellyfish are one of the earliest example of animal that actively regulate swimming, but the mechanisms governing the locomotion are still a matter of research. Jellyfish obtain locomotion by activating the subumbrellar muscle layer. Sensory inputs trigger the contraction of the bell and the fluid-structure interaction effects driving locomotion. These have been extensively studied, whereas a representation of the full neuro-mechanical locomotion chain, with focus on the actuation-locomotion dynamics, has not been proposed yet. A model of such a complex multi-physical phenomenon would be informative for several purposes, ranging from the comprehension of behavioral aspects to the design of soft actuators and bio-inspired devices. In this regard, we propose a computational framework to address the coupled electrophysiological, elastic, and fluid aspects of the locomotion of the Scyphozoan group. This relies on the sequential coupling of segregated solvers, such that each sub-problem can be addressed with the most computationally effective technique. The spatial discretization is addressed by isogeometric analysis for the electrophysiological and elastic sub-problems, and by finite differences for the fluid sub-problem. The active strain approach allows to distribute the active contraction of radial and coronal muscle fibers following the biological architecture.

The inherent multi-scale nature of the model is addressed by means of a nested grid approach and multiple time-advancement lines. In view of a reasonable computational effort, we enforce the hypothesis of axial symmetry limiting the number of degrees of freedom used in the simulations. The effectiveness of the scheme employed for each sub-problem is verified against different test-cases of engineering and biologic inspiration. Finally, we carry out an extensive comparison between the simulation output and the in-vivo measurements on a 3-cm specimen of *Aurelia Aurita*.

1. Introduction

Jellyfish have extensively played as inspirational test-cases for building bio-inspired and bio-hybrid robotic actuators [1–3]. Their inherent propulsive features make the Medusozoan ancestor a perfect model for drafting engineered solutions for soft actuators and

* Corresponding author.

E-mail address: alessandro.nitti@poliba.it (A. Nitti).

<https://doi.org/10.1016/j.apm.2023.08.003>

Received 28 March 2023; Received in revised form 28 July 2023; Accepted 2 August 2023

Available online 9 August 2023

0307-904X/© 2023 The Author(s). Published by Elsevier Inc. This is an open access article under the CC BY-NC-ND license (<http://creativecommons.org/licenses/by-nc-nd/4.0/>).

soft swimmers [4,5]. The latter are employed for monitoring and exploration purposes [6], by virtue of their superiority over hard devices in the maneuverability in narrow spaces and robustness under extreme pressure. This work proposes a multiphysics model for elucidating the actuation-locomotion relations of oblate jellyfish species in order to advance the comprehension of some behavioral aspects and possibly provide further guidelines for the design of modern soft actuators.

The jellyfish propulsion results from the alternation of the contraction of thin muscle bundles in the subumbrellar cavity and the shape recovery driven by the elastic energy stored in the Mesoglea, an extracellular matrix composed of collagen fibers. The flow field resulting from the volume change in the subumbrellar cavity and the vortices shed from the bell margin contribute to generate thrust. From a biologic perspective, the rowing locomotion of oblate species has proven an extraordinary low cost of transport in the low-speed cruising regime, thanks to the additional thrust obtained in the passive elastic recovery phase without extra metabolic cost [7]. The locomotion efficiency is further enhanced when considering that the active tissue contraction only comes from a single muscle layer lining the subumbrellar cavity [8]. These features endow oblate jellyfish with a simple and efficient propulsion system without recurring to agonist-antagonist muscle dynamics. The latter requires more sophisticated engineering solutions, generally used in a hard robotics design environment. Jellyfish also exhibit an inherently simple neuro-muscular architecture. All medusozoans present a distributed nervous system composed by several neuron networks located over the bell, the tentacles, and the endoderm (the part supplying the digestive and respiratory functions). In Scyphozoans the neuronal stimulation comes from the Rhopalia, which consist of sensory structures distributed around the bell margin [9], and it is transmitted to the innervated muscle bundles. Current advances in experimental neurobiological techniques allowed to dissect the electrophysiological functionalities and consequently draw behavioral considerations [10–13].

A step towards the effective and systematic design of jellyfish-inspired swimmers can be taken by drafting the functional relationships between actuation and locomotion features, which are not fully understood. This is certainly necessary to implement a forward-inverse design strategy, by which a hierarchical biologic function is unpacked into consequential events and replicated by simple engineering solutions [14].

Significant advances in the comprehension of jellyfish locomotion mechanisms came from the analysis of the interaction of the unsteady flow field and the body's elastic response. Both state-of-the-art experimental measurements [15,16,7] and time-resolved multiphysics simulations [17–19] played a crucial role in elucidating the Fluid-Structure Interaction (FSI) process in jellyfish propulsion. Nevertheless, locomotion performance have been assessed neglecting the efficiency of the actuation mechanisms in the total energy balance. This might lead to a limited perspective on the propulsion scenario [20]. A thorough understanding of the energy partitioning in the actuation-locomotion framework can also lead to a fair comparison with artificially actuated robots [4]. In this connection, a neuro-mechanical computational model can play as a cost-effective platform to draw the necessary energetic estimates. In this work, we propose a computational tool to explore the actuation-locomotion scenario of an oblate jellyfish. The FSI problem of jellyfish-like swimmers has been tackled with successful implementations [17,18,21] which brought to light many useful insights about their behavior. However, most of these numerical simulations coped with the muscle actuation by applying a time-varying tension on the outer surface of the jellyfish bell. In the pursuit of a biophysically realistic framework we couple a fluid-structure interaction system with an electrophysiological activation model which aims at replicating the space-time pattern of neuronal stimulation and the consequent muscle excitation. The product of this numerical experiment is an actively-swimming jellyfish, whose propulsive features are only dictated by the neuromuscular organization and the activation pattern of the pacemaker cells in the Rhopalia. Both muscle activation parameters and material properties have been tuned to match in-vivo measurements. Most of the biological features replicated by the model are abstracted from the group Scyphozoa, and in particular from the genus *Aurelia*. Scyphozoans differ from Hydrozoans and Cubomedusae by morphological, behavioral and reproductive features, although several sub-classes do not fulfill this categorization. To the best of our knowledge, a comparably sophisticated modeling approach is currently under development for multiphysics cardiac simulations [22,23], where the replication of pathological states requires a mutual connection between electrophysiological features and fluid pumping activity.

The excitation of the neuromuscular tissue is addressed by the monodomain approach [24], which results in a reaction-diffusion Partial Differential Equation (PDE), that must be solved over a surface representing the epitheliomuscular tissue layer lining the subumbrellar cavity [16]. The reaction effects are driven by an Hodgkin-Huxley type neuron model, specifically tailored for Scyphozoans [25]. The electrophysiological activity drives the active contraction of the subumbrellar muscles, which in turn is described by an Active Strain (AS) approach [26], in light of an accurate and realistic representation of the muscular actuation. The AS method is based on the multiplicative decomposition of the deformation gradient into an active and a passive part, with the former resulting from an arbitrary combination of coronal and radial fiber stretch. Conversely, the passive strain, mimicking the elastic response of the Mesoglea, follows a hyperelastic strain energy function. The electrophysiological and mechanical problems are numerically tackled by an isogeometric approach [27]. Isogeometric analysis (IgA) proposes a new computational paradigm for a direct integration of Computer Aided Design and Galerkin-based analyses. Within an isoparametric framework, IgA allows to adopt the spline functions used to define the geometry as basis functions for the solution. Among the fundamental advantages brought by NURBS-based IgA, in this context we count on the superior accuracy guaranteed by the high regularity of basis functions with respect to standard Lagrange polynomials employed in finite element analyses. These advantages take place in the approximation of sharp action potential waves, as well as in the solution of non-linearly elastic problems with limited locking effects [28,27].

The flow field is resolved by means of a direct numerical simulation approach over a staggered Cartesian grid. The incompressible Navier-Stokes equations are discretized by second-order accurate centered differences and solved following the fractional step scheme [29]. This approach allows to preserve circulation and kinetic energy in absence of time-differencing errors and viscosity [30], making it an ideal choice for solving the complex vortex dynamics arising from the rowing propulsion. The computational scenario is completed by the Immersed-Boundary (IB) treatment used to enforce the fluid-solid interface condition without cumbersome mesh

adaptation procedures. Following the approach presented by [31], the Eulerian forcing field necessary to get the no-slip condition is obtained on Lagrangian markers laying on the immersed interface in the form of a volume force field, and then transferred to the Eulerian nodes. Information at the Lagrangian marker location is interpolated by means of a Moving-Least Squares (MLS) method [32,33], which is acknowledged to attenuate spurious oscillations of hydrodynamic loads for moving interfaces, while preserving second-order accuracy in space.

The inherent multiphysic and multi-scale nature of the modeled electrophysiological and mechanical phenomena would result in a discrete implementation with a prohibitive number of degrees of freedom, requiring for exascale computing solutions. As a first three-way coupled model we restrict the solution fields to be axisymmetric, such that multiple swimming cycles can be obtained with a limited number of degrees of freedom. In the core of the manuscript it will be highlighted that within the appropriate subset of the parameter space the axisymmetric assumption leads to a realistic representation of the forward locomotion. The key novelty of the present work lies in the fully coupled framework including fluid-structure-electrophysiology interactions and the related axisymmetric formulation. In light of the heterogeneity of the applied methodologies, this paper only emphasizes key modeling aspects. A thorough verification and validation campaign is presented for each sub-problem, individually. Subsequently, the kinematics of our active jellyfish model is compared with the in-vivo measurements of a 3 cm Aurelia Aurita specimen [7], showing a good agreement. Additionally, we explore different muscular activation patterns to assess the effect of the contractility pattern on the propulsion features.

The manuscript is organized as follows: section 2 provides a description of the designed mathematical model and the simplifications with respect to the biological scenario. Elucidations on the jellyfish zoological features are included. Section 3 brings a description of the numerical techniques used to solve the partial differential equations drafted in section 2. The implementation of each sub-solver is verified and discussed in Appendix A by a broad set of benchmark problems. Section 4 presents a detailed comparison of the fully coupled jellyfish simulations with the available experimental data and discusses the output of the exploration of the actuation parameter space. Eventually, conclusions are drawn in section 5.

2. Mathematical model

Two reference frames are used in the formulation of the differential equations occurring in the present model: a Cartesian frame, defined by the base vectors $\{e_1, e_2, e_3\}$, and a convective curvilinear frame, locally identified by the covariant base vectors $\{g_1, g_2, g_3\}$. The former refers to the directions $\{x, y, z\}$, whereas the latter to the convective coordinates $\{\theta^1, \theta^2, \theta^3\}$. The sketch in Fig. 1 shows both reference frames as well as the domain topology for the electrophysiological, elastic, and fluid sub-problems.

2.1. Body geometry and kinematics

Following the assumption of an axisymmetric deformation field, any radial section along the axis of symmetry is assumed to remain planar under axisymmetric loads. However, any radial displacement induces a tangential strain, therefore an out-of-plane component of strain and of the associated stress must be considered [34]. A point in the body continuum can be identified in the Cartesian frame by the position vector r . Then, the covariant tangent base vectors are obtained by $g_i = \partial r / \partial \theta^i$. We emphasize that the bases of the curvilinear frame are neither orthonormal, nor unitary.

The assumption of axisymmetric displacement field lets the curvilinear coordinate θ^3 describes a circumference. Consequently, it yields:

$$r = r \cos(\theta^3/r) e_1 + r \sin(\theta^3/r) e_3 + y e_2, \tag{1}$$

$$g_3 = -r \sin(\theta^3/r) e_1 + r \cos(\theta^3/r) e_3. \tag{2}$$

The metric tensor of an arbitrary point in the solid continuum is defined by the first fundamental form of surfaces:

$$G_{ij} = g_i \cdot g_j. \tag{3}$$

The axial symmetry yields the coefficients:

$$G_{\alpha\beta} \neq 0, \quad G_{\alpha 3} = G_{3\alpha} = 0, \quad G_{33} = r^2. \tag{4}$$

When expressing strain and stress variables as a function of the metric tensor coefficients, Eq. (4) allows a fully curvilinear formulation without the need for coordinate transformations. The tensor deformation gradient is consistently defined as:

$$F = g_i \otimes \hat{g}^i, \tag{5}$$

where the symbol $(\hat{\cdot})$ indicates a quantity in the reference configuration, Ω_{s0} , and the superscript refers to contravariant vectors. A sketch of the reference configuration is illustrated in Fig. 3 (b). The Green–Lagrange strain tensor is assumed as finite strain measure:

$$E = \frac{1}{2} (FF^T - I) = E_{ij} \hat{g}^i \otimes \hat{g}^j, \tag{6}$$

which yields the non-zero strain components:

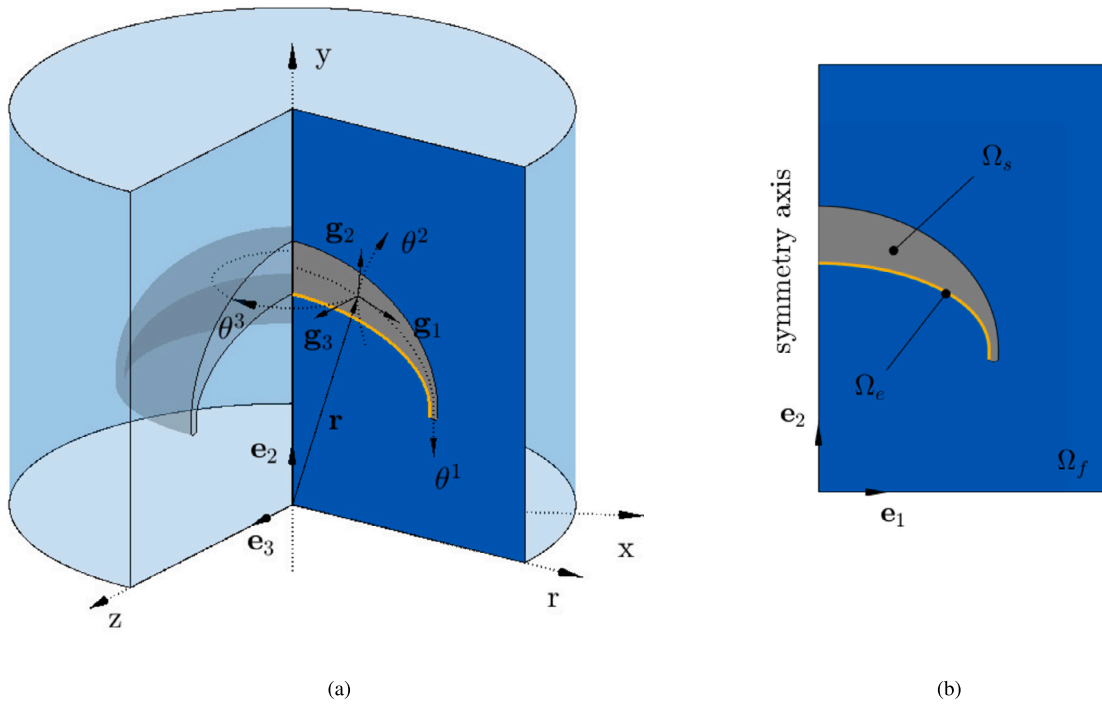


Fig. 1. Sketch of the Cartesian $\{x, y, z\}$ and the convective curvilinear $\{\theta^1, \theta^2, \theta^3\}$ coordinate systems used for the mathematical formulation (a). Summary outline of each sub-domain topology (b): the blue region (Ω_f) covers the fluid domain, the gray area (Ω_s) is the solid domain, the yellow line (Ω_e) represents the electrophysiological domain.

$$E_{\alpha\beta} = \frac{1}{2} (G_{\alpha\beta} - \hat{G}_{\alpha\beta}), \tag{7}$$

$$E_{33} = \frac{1}{2} (r^2 - \hat{r}^2). \tag{8}$$

Local deformations are expressed in terms of the right Cauchy–Green deformation tensor, defined on the contravariant base vectors:

$$\mathbf{C} = \mathbf{F}\mathbf{F}^T = G_{ij} \hat{\mathbf{g}}^i \otimes \hat{\mathbf{g}}^j. \tag{9}$$

2.2. Constitutive modeling of the solid phase

The elastic properties of the jellyfish bell, here discretized over the mechanical domain Ω_s (Fig. 1b), play a crucial role in the determination of the FSI dynamics. Regardless of the genus, the Mesoglea, a gelatinous substance comprised of randomly oriented collagen fibers and proteins networks [35], makes up the majority of jellyfish volume [36]. It provides structural support and stores the strain energy released in the elastic recoil stage. The collagen fibers form a network which varies from one species to another. This is the reason for jellyfish Mesoglea exhibiting quite different elastic properties. Many prior studies indicate that the elastic modulus of Mesoglea varies over a wide range of magnitude [37,38]. For instance, Demont and Gosline [39] found that intact jellyfish bell of the species *Polyorchis penicillatus* has a Young’s modulus between 400 and 1000 Pa. Megill et al. [37] found the stiffness of the Mesoglea of the same specimen to be 350 Pa in compression while the softer joint Mesoglea has stiffness of 50 Pa. We model the solid phase within Ω_s as an homogeneous isotropic medium which takes the elastic properties of the Mesoglea. The elastic parameters are tailored accordingly to the Mesoglea measurements on the *Aurelia Aurita*. The *Aurelia Aurita* was found to have a water content of 96.3% with a standard deviation of 0.57% [40]. Hence, a weakly compressible constitutive law is considered suitable for the scope of the work. Specifically, we adopt a Neo-Hookean strain energy density function [41]:

$$\Psi(\mathbf{C}) = c_{10} (I_1 I_3^{-1/3} - 3) + K(J - 1)^2, \tag{10}$$

where $I_1 = \text{tr}(\mathbf{C})$ and $I_3 = \det(\mathbf{C})$ denote the first and third invariants of the right Cauchy–Green deformation tensor \mathbf{C} and $J = \det(\mathbf{F})$ is the Jacobian of the deformation gradient tensor. The parameters c_{10} and K represent the shear and the bulk moduli. Following the tension-compression tests carried out by [37], we assume $c_{10} = 400$ Pa and $K = 5.0 \times 10^4$ Pa. The bulk modulus K is chosen as an arbitrary high value to get minimal volume changes; this assumption will be numerically verified in sub-section Appendix A.2. In the range of physiological muscle contraction frequency (0.2 ÷ 0.5 Hz) macro-rheological measurements [42] show that the Mesoglea exhibits an elastic shear modulus ten times larger than the viscous shear modulus. The viscoelastic response of the Mesoglea is thus neglected.

We adopt a total Lagrangian description (see section 3), which relies on the second Piola-Kirchhoff stress tensor \mathbf{S} , and on the fourth-order material tensor \mathbf{C} . They are defined on the covariant base vectors as:

$$\mathbf{S} = S^{ij} \hat{\mathbf{g}}_i \otimes \hat{\mathbf{g}}_j, \tag{11}$$

$$\mathbf{C} = C^{ijkl} \hat{\mathbf{g}}_i \otimes \hat{\mathbf{g}}_j \otimes \hat{\mathbf{g}}_k \otimes \hat{\mathbf{g}}_l. \tag{12}$$

The above contravariant coefficients can be obtained by derivation of the strain energy density with respect to the Cauchy-Green deformation tensor:

$$S^{ij} = 2 \frac{\partial \Psi}{\partial C_{ij}}, \tag{13}$$

$$C^{ijkl} = 4 \frac{\partial^2 \Psi}{\partial C_{ij} \partial C_{kl}}. \tag{14}$$

The strain energy function defined in Eq. (10) yields:

$$S^{ij} = 2c_{10} I_3^{-1/3} \left(\hat{G}^{ij} - \frac{1}{3} I_1 \bar{C}^{ij} \right) + 2K \bar{C}^{ij} (J^2 - J), \tag{15}$$

$$C^{ijkl} = -\frac{4}{3} c_{10} I_3^{-1/3} \left[\hat{G}^{ij} \bar{C}^{kl} + \hat{G}^{kl} \bar{C}^{ij} - \frac{1}{3} I_1 \bar{C}^{ij} \bar{C}^{kl} - \frac{1}{2} (\bar{C}^{ik} \bar{C}^{jl} + \bar{C}^{il} \bar{C}^{jk}) \right] + 2KJ [(2J - 1) \bar{C}^{ij} \bar{C}^{kl} - (J - 1) (\bar{C}^{ik} \bar{C}^{jl} + \bar{C}^{il} \bar{C}^{jk})], \tag{16}$$

where \bar{C}^{ij} are the components of the inverse of tensor \mathbf{C} : $\bar{C}^{ij} = [C^{ij}]^{-1}$.

2.3. Weak formulation for elasticity

We model the jellyfish bell as a hyperelastic continuum defining the total energy of the body, that is a function of the displacement field \mathbf{u} . According to classic results in continuum mechanics [43], the response of the body is such that the total energy is always minimal and, since we assume axisymmetric conditions, invariant with respect to the coordinate θ^3 , leading to the following form of the principle of virtual power:

$$\delta \Pi(\mathbf{u}, \delta \mathbf{v}) = 2\pi \int_{\Omega_{s0}} \rho_s \frac{\partial^2 \mathbf{u}}{\partial t^2} \cdot \delta \mathbf{v} \hat{r} dS + 2\pi \int_{\Omega_{s0}} \mathbf{S} : \delta \hat{\mathbf{E}} \hat{r} dS - 2\pi \int_{\partial \Omega_{s0}} \mathbf{t}_0 \cdot \delta \mathbf{v} \hat{r} dL = 0 \quad \forall \delta \mathbf{v}, \tag{17}$$

where dS and dL represent the infinitesimal area and arc-length in the reference configuration Ω_{s0} , respectively. In Eq. (17), we recognize three terms: the inertia of the system relying on the bell density ρ_s and on the acceleration, the stress expressed in terms of the second Piola-Kirchhoff stress tensor \mathbf{S} deriving from the elastic energy $\Psi(\mathbf{C})$ (as shown in the previous section), and the tractions \mathbf{t}_0 on the boundary of the solid body $\partial \Omega_{s0}$ depending on the action of the flow field. Each of them is work-conjugate with the virtual velocity $\delta \mathbf{v}$, or the virtual strain rate tensor [43]:

$$\delta \hat{\mathbf{E}} = \frac{1}{2} (\delta \hat{\mathbf{F}}^T \mathbf{F} + \mathbf{F}^T \delta \hat{\mathbf{F}}) \quad \text{with} \quad \delta \hat{\mathbf{F}} = \frac{\partial \delta \mathbf{v}}{\partial \theta^i} \otimes \hat{\mathbf{g}}^i, \tag{18}$$

providing an equation for each axisymmetric velocity field compatible with the Dirichlet boundary conditions. We solve such set of nonlinear equations by means of the Galerkin method. We remark that, as in plane-strain conditions, the axisymmetric virtual velocity field has only two non-zero components. However, the normal out-of-plane components of the stress and strain rate tensors are non-null, actively contributing to the total virtual power.

2.4. Muscle activation model

In both oblate and prolate jellyfish the muscle cells are mostly located in the marginal part of the endothelial area, and absent in the center, where the mouth is located. In most Scyphozoan and Hydrozoan, muscle fibers are oriented in radial and coronal bundles. During the contraction phase in forward swimming, the coronal muscles seem to provide predominant contraction with respect to the radial ones [44]. Radial muscles are thought to be mostly involved in maneuvering [45,46] operations. However, the physiological role of these muscle bundles and their interplay in locomotion has not been fully understood. Coronal muscles are innervated by the Motor Nerve Net (MNN), which is a through-conducting nerve bundle responsible for high-conduction speed action potentials within each swimming cycle [47,45]. Conversely, the radial muscle are mostly innervated by the Diffuse Nerve Net (DNN), a secondary net conducting slower electrophysiological waves. Although no coupling exists between radial and coronal muscle layers [45], both successive and simultaneous occurrence of MNN and DNN waves have been recorded for several Scyphozoans [11,48]. Apart from this, behavioral and anatomical evidences suggest that a single Rhopalium can activate both the MNN and the DNN in response to a strong sensory input [49,50] and that the DNN can exercise a modulatory control on the action potentials. As a simplifying assumption, we assume the radial and coronal muscle layers to be governed by the same nerve net, although different fiber stretching magnitudes are allowed. Thus, the muscle contraction waves are generated by the same electrophysiological pulse, but different contraction levels can be achieved. This can lead to a biologically-aware correlation between actuation pattern and locomotion performance.

From the cytological perspective, subumbrellar muscle fibrils (called myofibrils) are only restricted to epithelial cells in medusozoan. These cells, consequently termed epitheliomuscular cells, are typically distributed over a single cell layer, meaning that the myofibrils available to generate force for bell contraction are limited in depth and cross-sectional area [51].

We propose the implementation of such a muscular architecture by means of the active strain approach [52,53]. This allows to retrieve a realistic balance between actively contracting and passive part of the body in terms of volume fraction, as well as to disentangle the contribution of radial and coronal muscles in forward swimming.

The active strain approach is built on the multiplicative decomposition of the deformation gradient tensor into an elastic part \mathbf{F}_e and an active part \mathbf{F}_a :

$$\mathbf{F} = \mathbf{F}_e \mathbf{F}_a. \tag{19}$$

A schematic representation of this decomposition can be found in Fig. 1 of reference [54]. The active deformation \mathbf{F}_a mimics the macroscopic effects of the myofibril shortening driving the tissue contraction. In the present work, the instantaneous active gradient is prescribed by a phenomenological law which dictates the activation parameters embedded in \mathbf{F}_a . The explicit expression of \mathbf{F}_a is presented in the following of the present section. It is worth pointing out that \mathbf{F}_e and \mathbf{F}_a are not given by the gradient of a vector map. Kinematically, the active deformation leads to an intermediate non-compatible configuration which is subsequently relaxed towards the final configuration by the elastic response. Accordingly, \mathbf{F}_a is defined by the tensor product over base vectors in the reference configuration:

$$\mathbf{F}_a = F_a^{ij} \hat{\mathbf{g}}_i \otimes \hat{\mathbf{g}}_j, \quad \mathbf{F}_a^{-1} = \bar{F}_{a,ij} \hat{\mathbf{g}}^i \otimes \hat{\mathbf{g}}^j. \tag{20}$$

Considerations about the thermodynamic consistency of the active strain approach can be found in [55,54]. In this work, the elastic strain energy Ψ_e is thought as a function of the elastic part of the right Cauchy-Green deformation tensor \mathbf{C}_e :

$$\Psi_e = \Psi_e(\mathbf{C}_e), \tag{21}$$

which is defined following the deformation gradient split:

$$\mathbf{C} = \mathbf{F}_a^T \mathbf{C}_e \mathbf{F}_a. \tag{22}$$

The purely elastic quantities (denoted by the subscript “e”), as well as the elastic and active deformation gradient tensors, are all defined with respect to the reference configuration. We address the quantification of the determinant of the two parts of the tensor deformation gradient separately. Namely, for $J = J_e J_a$, we prescribe $J_a = 1$ by properly building the active deformation gradient, whereas J_e follows up from the choice of the bulk modulus K . The second Piola-Kirchhoff stress tensor is expressed as a function of the active deformation tensor. By exploiting the chain rule and the relation between the deformation tensor and its elastic counterpart (22), one can get the coefficient form:

$$S^{ij} = \frac{1}{2} \bar{F}_{a,uvp} \bar{F}_{a,zs} \hat{G}^{sj} (S_e^{pz} \hat{G}^{wi} + S_e^{pi} \hat{G}^{wz}), \tag{23}$$

where S_e^{pz} , S_e^{pi} are the contravariant coefficients of the elastic part of the tensor \mathbf{S} , and $\bar{F}_{a,uvp}$, $\bar{F}_{a,zs}$ are the coefficients of the inverse of the active deformation gradient tensor \mathbf{F}_a . Here \mathbf{F}_a is assumed to be independent from the elastic response of the body [54]. The expression of the tangent material tensor can be likewise obtained:

$$\mathbb{C}^{ijkl} = \frac{1}{4} \bar{F}_{a,uvp} \bar{F}_{a,zs} \bar{F}_{a,gh} \bar{F}_{a,nm} \hat{G}^{sj} \hat{G}^{ml} [\hat{G}^{gk} (C_e^{hnpz} \hat{G}^{wi} + C_e^{hnpi} \hat{G}^{wz}) + \hat{G}^{gn} (C_e^{hkpz} \hat{G}^{wi} + C_e^{hkpi} \hat{G}^{wz})]. \tag{24}$$

The details of the derivation of the latter expressions are presented in [54]. Eqs. (23) and (24) provide the expressions of the stress and material tensors for an active tissue with a prescribed active deformation gradient. These expressions hold in any three-dimensional domain, and can be easily traced to the particular case of an axisymmetric problem.

Taking advantage of the reference frame depicted in Fig. 1 (a), the active part of the tensor deformation gradient is built such that the local fiber orientation matches the convective curvilinear frame: the natural orientation of radial and coronal muscle fibers follows the base vectors \mathbf{g}^1 and \mathbf{g}^3 , respectively. Thus, \mathbf{F}_a takes the form:

$$\mathbf{F}_a = \mathbf{I} - \gamma [a_1 (\hat{\mathbf{g}}^1 \otimes \hat{\mathbf{g}}^1) + a_3 (\hat{\mathbf{g}}^3 \otimes \hat{\mathbf{g}}^3)] + \gamma_2 (\hat{\mathbf{g}}^2 \otimes \hat{\mathbf{g}}^2), \tag{25}$$

where γ is a smooth activation function of space and time (it takes values between 0 and 1), depending on the excitation state and a_2 and a_3 are space-dependent material parameters controlling the intensity of the active contraction for radial and coronal muscle fibers. The muscle fibers are sketched in Fig. 2, which highlights the consistency of the definition (25) with the local reference frame. Although the decomposition of the deformation gradient is carried out all over the solid domain, the activation parameters are null throughout most of the body, except that within a thin layer (pink region in Fig. 2), which plays the role of the subumbrellar muscles. γ_2 controls the activation in the θ^2 direction, i.e. along the thickness. Despite no muscle fiber takes this orientation, this term is necessary to fulfill the incompressibility constraint of the active part. Bringing the terms of Eq. (25) on the same basis, the coefficient equation for \mathbf{F}_a yields:

$$F_a^{ij} = \hat{G}^{ij} - \gamma (a_1 \hat{G}^{1i} \hat{G}^{1j} + a_3 \hat{G}^{3i} \hat{G}^{3j}) + \gamma_2 \hat{G}^{2i} \hat{G}^{2j}. \tag{26}$$

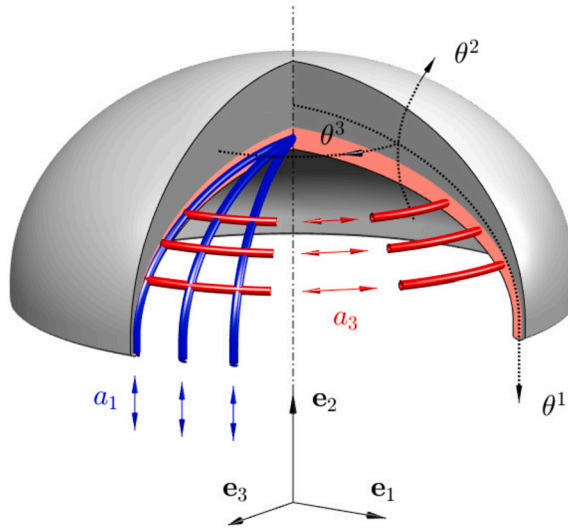


Fig. 2. Sketch of the fiber orientation for coronal (red) and radial (blue) muscles within the body continuum. The pink area is the subset of the computational domain where the activation parameters take non-zero values, representing the subumbrellar muscle layer. Conversely, the rest of the domain provides a purely passive response. The proportion between these areas follows an illustrative purpose only.

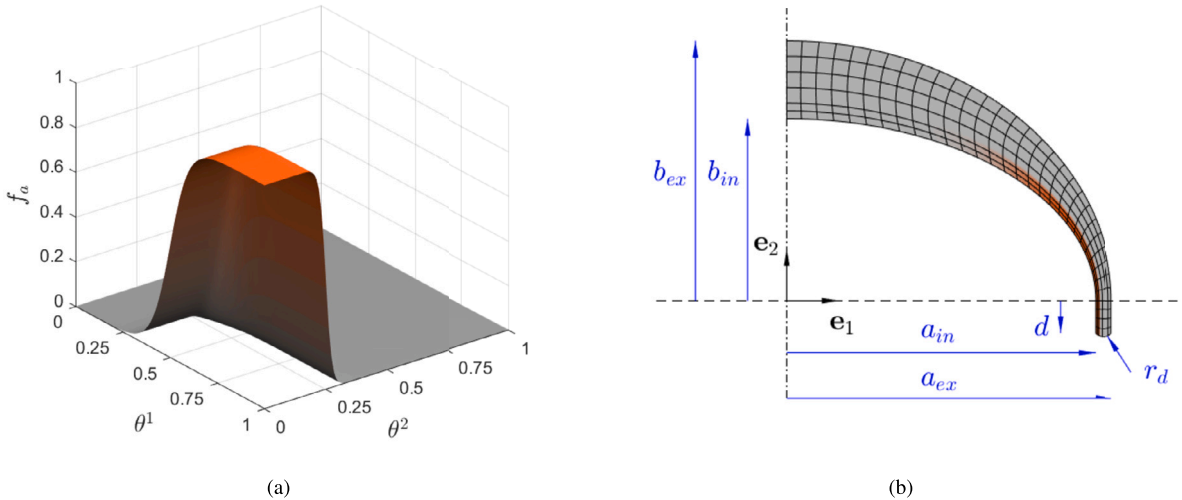


Fig. 3. Spatial distribution of the activation pattern f_a used to build the active deformation gradient (25), visualized in the NURBS parametric space (a). NURBS patch used as computational domain of the structural problem with the relevant geometric dimensions (b). Black lines denote the element edges for IgA, whereas the orange region displays f_a in the physical space.

The volume-preserving assumption about the active deformation, i.e., $J_a = |F_a^{ij}| / |\hat{G}^{ij}| = 1$, allows to compute γ_2 as:

$$\gamma_2 = \frac{-\gamma (a_1 \hat{G}^{11} + a_3 \hat{G}^{33} - \gamma a_1 a_3 \hat{G}^{11} \hat{G}^{33})}{(\gamma a_3 \hat{G}^{33} - 1) (\gamma a_1 (\hat{G}^{12})^2 + \hat{G}^{22} - \gamma a_1 \hat{G}^{11} \hat{G}^{22})}. \tag{27}$$

The activation field is described in the parametric space associated to the NURBS geometry by an hyperbolic tangent function scaled by the maximal activation values $\{\hat{a}_1, \hat{a}_3\}$, namely:

$$a_1(\theta^1, \theta^2) = \hat{a}_1 f_a, \tag{28}$$

$$a_3(\theta^1, \theta^2) = \hat{a}_3 f_a, \tag{29}$$

$$f_a(\theta^1, \theta^2) = \frac{1}{4} [1 - \tanh(w_2(\theta^2 - \delta_2))] [1 - \tanh(w_1(\delta_1 - \theta^1))], \tag{30}$$

with $w_2 = 40.0$, $w_1 = 10.0$, $\delta_1 = 0.55$, and $\delta_2 = 0.2$. We implicitly assume that the convective coordinates (θ^1, θ^2) in the parametric space take values within the interval $[0, 1] \times [0, 1]$. The extent of the active region is selected as a trade-off between zoological features

and numerical robustness necessities. Along the θ^1 direction f_a goes to zero due to the presence of the mouth and the stomach, where no muscular tissue overlaps [16], whereas along the θ^2 direction we employ the minimal extension necessary for the convergence of the numerical method. The pattern function f_a on both the parametric space and the physical space are displayed in Fig. 3. The peak activation values are the subject of the parameter exploration performed in section 4. The functional dependence of the activation function γ on the electrophysiological field variables is outlined in the following subsection.

2.5. Electrophysiological model and corresponding weak formulation

A well-outlined diversity can be pointed out in the architecture of the nervous system of Hydrozoan and Scyphozoan [9]; the present section provides a continuum model of the nervous system of Scyphozoan jellyfish. This class have neurons particularly clustered in the Rhopalia, where the most important sensory functions, such as sensing light, perceiving gravity, and triggering the electrophysiological activity, are executed [56]. Rhopalia are typically arranged in multiples of four, equally spaced over the bell margin [50]. The pacemaking function of specialized Rhopalial cells triggers the action potential diffused through the whole MNN [9], which in turn conducts synapses leading to a sequence of neuronal discharges [9,57]. It has been shown that Scyphozoan sensory input modulates the discharge rate of rhopalial pacemaking activity endowing these species with a wide range of contractility patterns [9]. Pacemaker cells are known to operate without direct communication among one another [12], thus the jellyfish can manage the temporal firing pattern to shape the action potential front and the consequent muscle contraction pattern. Non-symmetrical action potential fronts are known to provide turning maneuvers [46]. Despite these general features, a significant variation in the specifics of neuronal organization is found within the Medusozoan ancestor. We recall that in our computational model most of the zoological features are abstracted from the genus Aurelia. The correlation between MNN, DNN and sensory input is currently a matter of research. We neglect the presence of the DNN, and, as previously stated, we assume that both radial and coronal muscles are only activated by the action potential traveling through the MNN.

In most Scyphozoan, the neurons of the MNN have random orientation and they are electrically symmetric [9,50], resulting in an electrically homogeneous network. According to this feature, the electrophysiological activity of the body is modeled by means of the monodomain formulation [58]. The axial symmetry assumption entails a simultaneous firing of the pacemaker cells, which actually takes place in straight swimming. In view of the dimensionality reduction, a uniform instantaneous distribution of the action potential is assumed in the tangential direction. Simultaneous pacemaker discharges were found to produce independent excitation waves, that, when colliding, cancel out, owing to a state of mutual refractoriness in the area surrounding the collision [57]. Such a physiological feature allows to neglect the three-dimensional nature of the action potential pattern (i.e., the collision of spherical depolarization fronts) generated by the synchronous firing of multiple pacemakers. Thus, our axisymmetric model only describes the propagation of the action potential wave front in the radial direction, along a curvilinear abscissa on the subumbrellar profile (domain Ω_e , displayed in Fig. 1). Neumann boundary conditions are enforced to let the electrophysiological wave exit the domain with minimal reflections. The monodomain problem, built out of a reaction-diffusion partial differential equation and k ordinary differential equations, reads:

$$\begin{cases} C_m \frac{\partial v}{\partial t} - \nabla \cdot (\mathbf{D}\nabla v) + \chi i_{\text{ion}}(v, G_k) = \chi i_a, \\ \frac{dG_k}{dt} = \frac{G_{k\infty} - G_k}{\tau_k}. \end{cases} \tag{31}$$

This system presents the unknown scalar fields v and G_k , representing the transmembrane potential and the gating variables, respectively, whereas i_{ion} is the transmembrane ionic current. i_a denotes the applied external current field, \mathbf{D} is the conductivity tensor, and the coefficients χ and C_m are the surface-to-volume ratio and the transmembrane capacitance. The ODEs in system (31) provide the evolution of each gating variable, i.e., the instantaneous portion of cumulative membrane area covered by open ionic gates.

To obtain a weak formulation for a Galerkin-type discretization, one can multiply the PDE in (31) by all the admissible test functions ψ and integrating over the surface Ω_{e0} , representing the endothelial surface in the reference configuration. It yields:

$$2\pi \left(C_m \int_{\Omega_{e0}} \frac{\partial v}{\partial t} \psi \hat{r} dl - \int_{\Omega_{e0}} \nabla \cdot (\mathbf{D}\nabla v) \psi \hat{r} dl + \chi \int_{\Omega_{e0}} i_{\text{ion}}(v, G_k) \psi \hat{r} dl \right) = 2\pi \chi \int_{\Omega_{e0}} i_a \psi \hat{r} dl. \tag{32}$$

Using the Green’s identity and applying homogeneous Neumann boundary conditions to the diffusion term, it results in:

$$2\pi \left(C_m \int_{\Omega_{e0}} \frac{\partial v}{\partial t} \psi \hat{r} dl + \int_{\Omega_{e0}} \nabla \psi \cdot (\mathbf{D}\nabla v) \hat{r} dl + \chi \int_{\Omega_{e0}} i_{\text{ion}}(v, G_k) \psi \hat{r} dl \right) = 2\pi \chi \int_{\Omega_{e0}} i_a \psi \hat{r} dl. \tag{33}$$

The diffusion process takes place according to the axisymmetric hypothesis, therefore a consistent definition of the conductivity tensor must be adopted:

$$\mathbf{D} = D^{ij} \mathbf{g}_i \otimes \mathbf{g}_j, \tag{34}$$

with:

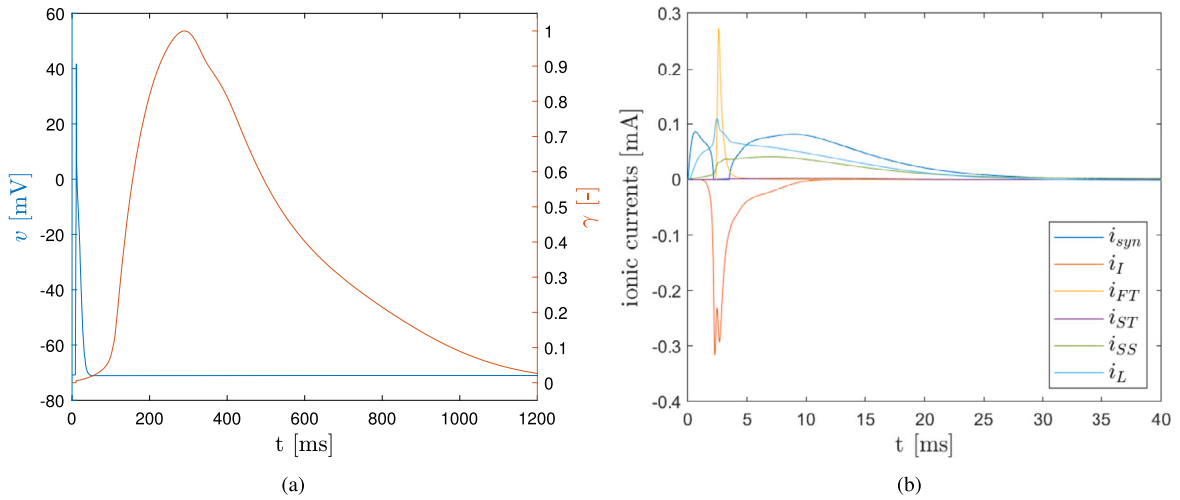


Fig. 4. Time traces of the transmembrane potential and activation function (a). Disentangled ionic currents (b) involved in the neuron model.

$$D^{ij} = \text{diag} [D_0, 0, D_0 r^2]. \tag{35}$$

D_0 represents the spatially uniform conduction coefficient. Following the previous equation, $D^{22} = 0$ since the diffusion process is assumed to take place over the surface defined by the in-plane base vectors \mathbf{g}_1 , and \mathbf{g}_3 . The other in-plane coefficients $D^{13} = D^{31}$ are set to zero too, for the problem to hold the axial symmetry. It is worth noting that the conductivity tensor depends on the local orientation of the base vectors to account for the mechano-electrical feedback arising from the body reconfiguration.

The dynamics of the ionic currents in Scyphozoan neurons has been modeled following the framework presented in [25]. In this study, the gating parameters have been fitted over experimental data from [13] by a least-squares procedure. Conversely, the parameters concerning the membrane capacitance and the Excitatory Post-Synaptic (EPS) current have been tuned such that the model can replicate both the action potential shape and the time-traces of different ionic currents [57]. Pallasdies et al. [25] proposed a Hodgkin-Huxley neuron model to be integrated into the discrete representation of the MNN, made up of a set of randomly oriented neurons that propagate the action potential from a neuron to the surrounding ones after a time delay. In our monodomain formulation, the signal propagates in the continuum accordingly to the diffusion coefficients. The synaptic current activates when the potential exceeds a predefined threshold. As the evolution of the potential upstroke is already included in the neuron model, we fix the threshold (-70.0 mV) close to the resting potential (-70.85 mV). Following the characterization of the ionic currents in [25], the implemented model distinguishes between a transient inward current (i_I), a passive leakage current (i_L), a steady-state outward current (i_{SS}) and a slow and a fast transient outward current (i_{ST} and i_{FT}):

$$i_{ion}(v) = i_I + i_{FT} + i_{ST} + i_{SS} + i_L + i_{SY}. \tag{36}$$

The experimentally observed synaptic rectification is also incorporated in the model, meaning that the voltage approaches the reversal potential ($+4$ mV) but does not reverse beyond. Provided the electrical symmetry of the MNN neurons, beyond this threshold the transmitter release into the synaptic cleft is assumed to produce a “synaptic reflux”, therefore a secondary excitatory postsynaptic potential, responsible for a delayed repolarization [57], is triggered. In accordance with multiple experimental measurements [59], the present neuron model provides a 30 ms absolute refractory period, which is sufficiently long to prevent repetitive firing triggered by the synaptic reflux. Time traces of the transmembrane potential and ionic currents are shown in Fig. 4 along with the activation function, described in (46). According to the Hodgkin-Huxley modeling approach, each current includes the product of two gating variables (one for the activation and one for the inactivation) whose exponents yield the probability of channel opening. Seven gating variables are thus considered:

$$i_I = g_I G_a^{1.77} G_b^{4.82} (v - E_I), \tag{37}$$

$$i_{FT} = g_{FT} G_c^{8.64} G_d^{2.51} (v - E_O), \tag{38}$$

$$i_{ST} = g_{ST} G_e^{3.85} G_f^{1.15} (v - E_O), \tag{39}$$

$$i_{SS} = g_{SS} G_g^{1.0} (v - E_O), \tag{40}$$

$$i_L = g_L (v - E_L). \tag{41}$$

Here $g_k, k \in \{I, FT, ST, SS, L\}$, are the peak conductances per unit area, $E_j, j \in \{I, O, L\}$, are the reversal potentials of the currents, $G_i, i \in \{a, b, c, d, e, f, g\}$, are the gating variables. The steady-state value of a gating variable $G_{i\infty}$ and the time constant τ_i are given by a logistic function with slope ρ_i and by a simple Gaussian distribution, respectively:

$$G_{k\infty}(v) = (1 + \exp((v_h)_k - v) / \rho_i)^{-1}, \tag{42}$$

$$\tau_k(v) = (C_b)_k + (C_a)_k \exp\left(\frac{-((v_m)_k - v)^2}{\sigma_k^2}\right). \tag{43}$$

Among the various constants, v_m and v_h are the maximal and the half-maximal voltage, respectively. By Eq. (42) one can infer that the dependence of the gating variables on the transmembrane potential v inherently makes the reaction term in the monodomain model nonlinear. This affects the choice of the suitable numerical scheme for the time discretization.

Following the aforementioned models and the experimental findings of [57], the voltage threshold for synaptic transmitter release is set to +20 mV. As long as the transmembrane potential achieve this threshold in the depolarization stage, excitatory postsynaptic currents (EPSCs) are triggered. The sum of individual EPSCs evoked in time yields the total synaptic current:

$$i_{EPSC}(t) = g_{SY} [1 - e^{-t/\tau_{rise}}] \left[a e^{-t/\tau_{fast}} + (1 - a) e^{-t/\tau_{slow}} \right] H(t) \max(E_{SY} - v, 0) \tag{44}$$

$$i_{SY} = \sum_{i=1}^n i_{EPSC}(t - t_i). \tag{45}$$

Here E_{SY} is the current’s reversal potential, a the fraction of fast decay and $H(t)$ the Heaviside step function. The maximum function accounts for the synaptic rectification [57]. The time constants τ_{rise} , τ_{rise} and τ_{rise} govern the rise and decay rate of the EPSC. All the parameters of the neuron model can be found in [25].

Quantitative observations about the space-time correlation between the electrical activity of the MNN and the muscle contraction pattern are still fairly limited. The duration of the muscle contraction was found to be a function of the bell diameter, indeed [60]. In Horridge et al. [61], experimental investigations on the Aurelia Aurita determined an approximate contraction duration of 1 s. This value was recently employed in high-fidelity simulations of the jellyfish turning [46], providing a satisfactory agreement with the experimental observations. Furthermore, it matches the experimental time range $0.2 \div 0.7$ s observed from muscle sheet recordings in several species [62,63]. The force generation mechanism in scyphozoan muscle fibers was early correlated to Calcium ion currents, likewise in striated muscle fibers of higher metazoans [64]. Muscle activation models based on Calcium dynamics have already been used for the simulation of Lamprey swimming [65], however, similarly detailed models are not available for jellyfish. To limit the complexity of the model, we propose a direct relation between one of the gating variables and the activation function although more refined formulations, such that Hill’s model [66], can be implemented to consider detailed physiological relations (e.g., the Frank-Starling law [67]) between the muscle stretch and stretch-rate, and the activation function γ [68]. We define the normalized muscle activation function γ by means of direct scaling of the dynamics of the gating variable G_a , associated to the transient inward current. The scaling is performed such that the contraction holds for approximately 1 s, and the contraction phase is more rapid than bell relaxation. As a result of the asymmetry in the timing of the two phases larger flow velocities are achieved during bell contraction than during bell relaxation [69]. Thus, the activation function takes the form:

$$\gamma(t, G_a) = \frac{1}{0.902} G_a (\eta t + \hat{t}(1 - \eta)), \tag{46}$$

where the scaling parameter η takes the value 1/140, and \hat{t} represents the time for which G_a exceeds the threshold 0.005. The parameters are chosen such that the duration of the muscle activity is in the range of a variety of jellyfish species (see Table 2 in [63]). A comparison of the time scale of the activation function and that of the transmembrane potential can be inferred from Fig. 4(a).

2.6. Fluid-dynamics model

The incompressible Navier-Stokes equations are solved in a cylindrical reference frame (domain Ω_f displayed in Fig. 1) under the assumption of axisymmetric flow. In view of this framework, the dimensionless continuity and momentum equations take the form:

$$\begin{cases} \frac{\partial q_1}{\partial r} + r \frac{\partial q_2}{\partial z} = 0, \\ \frac{\partial q_1}{\partial t} + \frac{\partial}{\partial r} \left(\frac{q_1^2}{r} \right) + \frac{\partial}{\partial y} (q_1 q_2) = -r \frac{\partial p}{\partial y} + \frac{1}{\text{Re}} \left[r \frac{\partial}{\partial r} \left(\frac{1}{r} \frac{\partial q_1}{\partial r} \right) + \frac{\partial^2 q_1}{\partial y^2} \right] + f_r, \\ \frac{\partial q_2}{\partial t} + \frac{1}{r} \frac{\partial}{\partial r} (q_1 q_2) + \frac{\partial q_2^2}{\partial y} = -\frac{\partial p}{\partial y} + \frac{1}{\text{Re}} \left[\frac{1}{r} \frac{\partial}{\partial r} \left(r \frac{\partial q_2}{\partial r} \right) + \frac{\partial^2 q_2}{\partial y^2} \right] + f_y, \end{cases} \tag{47}$$

where Re is the Reynolds number and the quantities $q_1 = rv_1$ and $q_2 = v_2$ denote the scaled radial and axial velocity components, respectively. With this expedient, the governing equations can be easily recast in a similar way to the Cartesian form [70]. When considering the bell diameter, hereafter referred as $2a_{ex}$, as characteristic length scale and the pacing frequency ϕ as characteristic time scale, the Reynolds number yields:

$$\text{Re} = \frac{4 \rho_f \phi a_{ex}^2}{\mu}, \tag{48}$$

where the frequency driving the bell deformation is equal to the frequency of electrophysiological pulses. Here ρ_f and μ represent the fluid density and dynamic viscosity, respectively.

In our study the fluid properties are kept fixed, therefore the Reynolds number and the driving pulse frequency are correlated parameters: once the frequency of the electrophysiological activation and the bell diameter are chosen, the Reynolds number is uniquely determined. Experimental measurements performed by [15] on both oblate jellyfish, such as the *Aequorea Victoria*, and prolate jellyfish (e.g., *Aglantha Digitale*), provided Reynolds number values in between 200 and 600 for centimeter-scale specimens ($2a_{ex} \approx 1 \div 6$ cm). Within this range, the vortex structures generated by axisymmetric bell strokes are noticed to be axisymmetric in many computational investigations [17,18,71], having considered axisymmetric bell deformations. In our model we consider $2a_{ex} = 3$ cm, $\phi = 0.5$ Hz. In conjunction with the fluid properties summarized in Table B.3, this yields $Re = 450$. It is worth pointing out that real jellyfish do not generate axisymmetric vortex rings, not even in this fluid-dynamic regime, due to the presence of tentacles and non-symmetric bell contractions.

The propulsion features have been widely recognized to be correlated with bell streamlining (or bell fineness ratio) and velum-diameter ratio [15,72]. Prolate medusae generally possess a large velum/diameter ratio and perform fast contractions, resulting in a rapid ejection of the fluid from inside their bell while entraining minimal fluid from outside the bell into their wake. Consequently, a clearly defined jet structure is produced. Conversely, oblate species derive only a small portion of thrust from jet propulsion. They provide slower contractions which produce prominent vortices at the bell margins mostly observed in rowing propulsion. As their bells expand, after each contraction, water rushes in, and it refills the bell in the form of a large vortex ring that rotates in the opposite direction of the ring created when the bell is contracted. According to [44], this classification based on the propulsion mechanism mostly complies with the distinction between Hydrozoans and Scyphozoans, despite paddling/rowing propulsion is observed in oblate hydromedusae as well [73]. There exist species that evade the distinction between prolate and oblate jellyfish in terms of propulsion mechanism. For instance, the *Aurelia Aurita* [74] and the *Aequorea Victoria* [75] have been found to exploit both rowing and jet propulsion mechanisms together.

2.7. Jellyfish geometry

Recent investigations have described the bell geometry as a solid made up from an extraumbrellar and a subumbrellar surface [76,18,77]. Following the parametrization introduced by [18], the axisymmetric profile of bell is delimited by the curves:

$$\frac{(r - r_c)^2}{a_{ex}^2} + \frac{(y - y_c)^2}{b_{ex}^2} = 1, \quad \frac{(r - r_c)^2}{a_{in}^2} + \frac{(y - y_c)^2}{b_{in}^2} = 1, \tag{49}$$

where the minor- and major semi-axis coefficients take the values: $b_{ex} = 0.8 a_{ex}$, $a_{in} = 0.948 a_{ex}$, $a_{in} = 0.46 a_{ex}$. The coordinate pair $\{r_c, y_c\}$ represents the location of the center of the ellipses. The major axis of the ellipse, a_{ex} , corresponds to half the bell diameter. Such a geometry was originally proposed by [56], and subsequently used by [18] as a sample representative of oblate rowing jellyfish, such as the *Aurelia Aurita*. The rear part of the bell is rounded by a circular arc of radius $r_d = 0.036 a_{ex}$. The elliptical profiles have been elongated by a distance $d = 0.14 a_{ex}$ to account for the flexible marginal flap encountered in many cnidarian species. Geometrical parameters are displayed along with the computational mesh in Fig. 3 (b).

Such a planar geometry \mathbf{X}_s is represented using a bivariate NURBS patch taking the tensor product of univariate NURBS functions and a linear combination with the control point coordinates $\hat{\mathbf{B}}_i$ [78]:

$$\mathbf{X}_s = \sum_{i=1}^{n_g} R_i(\theta^1, \theta^2) \hat{\mathbf{B}}_i, \tag{50}$$

where $R_i(\theta^1, \theta^2) = N_j(\theta^1)M_k(\theta^2)$ represents the tensor product structure and, consequently, the number of bivariate function is equal to the product of the number of univariate functions in the parametric directions θ^1 and θ^2 : $n_g = n_{g1} \times n_{g2}$. In our model, the two opposite edges of the parametric space, $\theta^2 = 0$ and $\theta^2 = 1$, represent the subumbrellar surface and the external surface, while the remaining two sides represent the straight segment coincident with the axis of symmetry and bell margin. Adopting this parametrization, the electrophysiological domain Ω_e – that is a subset of the mechanical domain Ω_s – is simply identified by:

$$\mathbf{X}_e = \sum_{i=1}^{n_g} R_i(\theta^1, 0) \hat{\mathbf{B}}_i = \sum_{j=1}^{n_{g1}} N_j(\theta^1) \hat{\mathbf{B}}_j. \tag{51}$$

In the IgA context the knot-insertion and the degree-elevation algorithms can be directly used to obtain analysis-suitable functions preserving both the geometry and the parametrization.

3. Numerical approach

The spatial discretization of the multiphysics problem follows a partitioned approach, by which different numerical techniques are employed for different sub-problems. We rely on a NURBS-based Isogeometric method for the solution of the electrophysiological and elastic sub-problems and a centered finite difference approach for the fluid sub-problem. The relevant details of the discretization techniques are reported in the present section, whilst their implementation is verified and discussed in Appendix A.

3.1. Isogeometric discretization for finite elasticity

We discretize the finite elasticity problem by means of an isogeometric Galerkin method in space, and by the generalized- α method in time. The body displacement and the virtual velocity fields are approximated by:

$$\mathbf{u} = \sum_{i=1}^{n_m} R_i(\theta^1, \theta^2) \hat{\mathbf{u}}_i(t), \tag{52}$$

$$\delta \mathbf{v} = \sum_{i=1}^{n_m} R_i(\theta^1, \theta^2) \delta \hat{\mathbf{v}}_i, \tag{53}$$

which, recast in the equivalent matrix notation, read:

$$\mathbf{u} = \left[\begin{array}{cc|cc} R_1(\theta^1, \theta^2) & 0 & \dots & 0 \\ 0 & R_1(\theta^1, \theta^2) & 0 & \dots \end{array} \middle| \begin{array}{cc} R_{n_m}(\theta^1, \theta^2) & 0 \\ 0 & R_{n_m}(\theta^1, \theta^2) \end{array} \right] \begin{pmatrix} \hat{u}_{1,1} \\ \hat{u}_{1,2} \\ \dots \\ \hat{u}_{n_m,1} \\ \hat{u}_{n_m,2} \end{pmatrix} = \mathbf{R} \hat{\mathbf{u}} \tag{54}$$

$$\delta \mathbf{v} = \left[\begin{array}{cc|cc} R_1(\theta^1, \theta^2) & 0 & \dots & 0 \\ 0 & R_1(\theta^1, \theta^2) & 0 & \dots \end{array} \middle| \begin{array}{cc} R_{n_m}(\theta^1, \theta^2) & 0 \\ 0 & R_{n_m}(\theta^1, \theta^2) \end{array} \right] \begin{pmatrix} \delta \hat{v}_{1,1} \\ \delta \hat{v}_{1,2} \\ \dots \\ \delta \hat{v}_{n_m,1} \\ \delta \hat{v}_{n_m,2} \end{pmatrix} = \mathbf{R} \delta \hat{\mathbf{v}} \tag{55}$$

To simplify the notation double indices are avoided in the control variable vectors. Substituting (55) in Eq. (17) and considering (54), one can derive $2 \times n_m$ equations, with n_m control points of the mechanical problem. Each of the resulting nonlinear equations corresponds to one variation of the finite-dimensional virtual velocity field:

$$\text{Res}_i = 2\pi \int_{\Omega_{s0}} R_{ki} \frac{\partial^2 u_k}{\partial t^2} \rho_s \hat{r} dS + \overbrace{2\pi \int_{\Omega_{s0}} \frac{1}{2} \left(\frac{\partial R_{mi}}{\partial \theta^a} \hat{g}_k^a F_{ml} + \frac{\partial R_{mi}}{\partial \theta^b} \hat{g}_l^b F_{mk} \right) S^{kl} \hat{r} dS}^{F_i^{int}} + \overbrace{-2\pi \int_{\partial\Omega_{s0}} R_{ki} t_{0,k} \hat{r} dL}^{F_i^{ext}} = 0 \quad i = 1, \dots, 2 \times n_m, \tag{56}$$

where the index i denotes the degree of freedom of the problem, while the indices $k, l,$ and m indicate the direction in space. In the latter equation we drop the functional dependence on the control variables and we adopt Einstein’s notation on summations. Moreover, we recall that the deformation gradient depends on the active strain, coupling the displacement field to the monodomain problem.

The generalized- α method is a nonlinear predictor-corrector time integration scheme, that updates the displacement control variables solving the residual equations (56) by means of the Newton’s method. Thus, the linearization of the first integral in (56) with respect to the acceleration control variables $\hat{a}_j = \partial^2 \hat{u}_j / \partial t^2$, wit $j = 1, \dots, 2 \times n_m$, is needed, yielding:

$$M_{ij} = 2\pi \int_{\Omega_{s0}} R_{ki} R_{kj} \rho_s \hat{r} dS \tag{57}$$

as well as the linearization of the second integral with respect to the displacement control variable \hat{u}_j :

$$K_{ij}(\hat{\mathbf{u}}) = 2\pi \int_{\Omega_{s0}} \overbrace{\frac{1}{2} \left(\frac{\partial R_{mi}}{\partial \theta^a} \hat{g}_k^a \frac{\partial R_{mj}}{\partial \theta^l} + \frac{\partial R_{mi}}{\partial \theta^b} \hat{g}_l^b \frac{\partial R_{mj}}{\partial \theta^k} \right) S^{kl} \hat{r} dS}^{D_{[\Delta \hat{\mathbf{u}}]} \delta \hat{\mathbf{E}} : \mathbf{S}} + 2\pi \int_{\Omega_{s0}} \overbrace{\left(\frac{\partial R_{mi}}{\partial \theta^a} \hat{g}_k^a F_{ml} + \frac{\partial R_{mi}}{\partial \theta^b} \hat{g}_l^b F_{mk} \right) \mathbb{C}^{klwq} \frac{1}{2} \left(\frac{\partial R_{wi}}{\partial \theta^q} + \frac{\partial R_{qi}}{\partial \theta^w} + \frac{\partial u_w}{\partial \theta^b} \frac{\partial R_{ri}}{\partial \theta^b} + \frac{\partial R_{wi}}{\partial \theta^f} \frac{\partial u_q}{\partial \theta^f} \right) \hat{r} dS}^{\delta \hat{\mathbf{E}} : D_{[\Delta \hat{\mathbf{u}}]} \mathbf{S}}. \tag{58}$$

Conversely, the hydrodynamic load depends only on time because of the adopted FSI scheme (see section 3.5). To integrate in time, we interpolate the displacements and accelerations between two successive time steps t_n and $t_{n+1} = t_n + \Delta t$ as follows:

$$\hat{\mathbf{u}}^\alpha = \alpha_f \hat{\mathbf{u}}^{n+1} + (1 - \alpha_f) \hat{\mathbf{u}}^n, \tag{59}$$

$$\hat{\mathbf{a}}^\alpha = \alpha_m \hat{\mathbf{a}}^{n+1} + (1 - \alpha_m) \hat{\mathbf{a}}^n, \tag{60}$$

where the velocity and the displacements at time step t_{n+1} are computed by the Newmark update:

$$\hat{\mathbf{v}}^{n+1} = \hat{\mathbf{v}}^n + \Delta t ((1 - \gamma) \hat{\mathbf{a}}^n + \gamma \hat{\mathbf{a}}^{n+1}), \tag{61}$$

$$\hat{\mathbf{u}}^{n+1} = \hat{\mathbf{u}}^n + \Delta t \hat{\mathbf{v}}^n + \frac{\Delta t^2}{2} ((1 - 2\beta) \hat{\mathbf{a}}^n + 2\beta \hat{\mathbf{a}}^{n+1}). \tag{62}$$

The convergence of the generalized- α method is regulated by the set of adopted coefficients, that, furthermore, defines the amount of numerical damping for high-frequency modes. In the present work, we adopt the following set of coefficients [79], defined as a function of the spectral radius of the iteration matrix ρ_∞ :

$$\alpha_m = \frac{2 - \rho_\infty}{1 + \rho_\infty}, \quad \alpha_f = \frac{1}{1 + \rho_\infty}, \quad \beta = \frac{(1 - \alpha_f + \alpha_m)^2}{4}, \quad \gamma = \frac{1}{2} - \alpha_f + \alpha_m. \tag{63}$$

In this work we follow the classical choice $\rho_\infty = 0.5$ [79], which allows to damp out spurious high frequency modes while preserving most of the natural ones.

When updating the displacements, we solve Eq. (56), computed with the variables interpolated at the time fraction α , in terms of acceleration by means of the Newton’s method. The update formula can be obtained exploiting the chain rule to differentiate with respect to acceleration:

$$\frac{d\mathbf{Res}^\alpha}{d\hat{\mathbf{a}}^{n+1}} \Delta \hat{\mathbf{a}}^{n+1} = -\mathbf{Res}^\alpha, \tag{64}$$

which reads, in index notation:

$$(\alpha_m M_{ij} + \alpha_f \beta \Delta t^2 K_{ij}(\hat{\mathbf{u}}^\alpha)) \Delta \hat{a}_j^{n+1} = -M_{ij} \hat{a}_j^\alpha - F_i^{int,\alpha} + F_i^{ext,\alpha}, \tag{65}$$

where $F_i^{int,\alpha}$ is the internal elastic power computed in term of displacements $\hat{\mathbf{u}}^\alpha$ and $F_i^{ext,\alpha}$ represents the hydrodynamic load extrapolated from the previous time step. As a starting guess for the Newton’s method, we employ a constant velocity predictor. For more details on the method, the reader is referred to [79,80]. In the present work, the classic Gauss–Legendre quadrature rule is employed to integrate the field variables over the elements. The linear system corresponding to Eq. (64) is solved via a standard LU decomposition with partial pivoting.

3.2. Isogeometric discretization for electrophysiology

The weak form of the monodomain model (33) is linear in the argument v except for the reactive term, which depends on the transmembrane potential itself:

$$v = \sum_{j=1}^{n_s} N_j(\theta^1) \hat{v}_j(t) \tag{66}$$

where the N_j basis function is obtained from the geometrical representation of the domain Ω_{0e} after a suitable mesh refinement and \hat{v}_j is the corresponding control variable with j varying from 1 to the number of degrees of freedom n_s . Substituting Eq. (66) in the weak form (33) and using the same basis function N_i to approximate the test functions:

$$\psi = \sum_{i=1}^{n_s} N_i(\theta^1) \hat{\psi}_i, \tag{67}$$

we get the discrete isogeometric counterpart of the monodomain PDE. The following system of equations is obtained:

$$C_m M_{ij}^e \frac{d\hat{v}_j}{dt} + K_{ij}^e \hat{v}_j + \chi (I_{ion})_i = \chi (I_a)_i \quad i = 1, \dots, n_s. \tag{68}$$

The matrices in the previous equation read:

$$M_{ij}^e = 2\pi \int_{\Omega_{e0}} N_i N_j \hat{r} dL, \tag{69}$$

$$K_{ij}^e = 2\pi \int_{\Omega_{e0}} \frac{\partial N_i}{\partial \theta^1} D^{11}(\theta^1) \frac{\partial N_j}{\partial \theta^1} \hat{r} dL, \tag{70}$$

$$(I_{ion})_i = 2\pi \int_{\Omega_{e0}} N_i i_{ion}(v, G_k) \hat{r} dL, \tag{71}$$

$$(I_a)_i = 2\pi \int_{\Omega_{e0}} N_i i_a(\theta^1) \hat{r} dL. \tag{72}$$

System (68) is discretized in time by a semi-implicit scheme, where the diffusion term is treated implicitly and the reaction term explicitly, as this is believed to provide a satisfactory compromise between efficiency and stability [81,54]. Indeed, the explicit treatment of the reaction term avoids the linearization of the ionic current at the cost of a restriction on the time step size due to the stability constraint.

In our implementation, the reaction term is discretized by means of an explicit second order Adams-Bashforth method, and the diffusion term is discretized by an implicit Crank-Nicholson method. The present scheme is outlined for the resolving time step $m + 1$, which refers to the discrete time $t^{m+1} = (m + 1)\Delta t_e$, with m being the discrete time counter and $\Delta t_e = t^{m+1} - t^m$ the constant time step size chosen for the electrophysiological problem:

$$C_m M_{ij}^e \frac{\hat{v}_j^{m+1} - \hat{v}_j^m}{\Delta t_e} + \frac{1}{2} K_{ij}^e (\hat{v}_j^{m+1} + \hat{v}_j^m) + \frac{3}{2} \chi (I_{ion})_i^m - \frac{1}{2} \chi (I_{ion})_i^{m-1} = \chi (I_a)_i^{m+1}, \tag{73}$$

which, rearranged for the time advancement, reads:

$$\left(C_m M_{ij}^e + \frac{\Delta t_e}{2} K_{ij}^e \right) \hat{v}_j^{m+1} = \left(C_m M_{ij}^e - \frac{\Delta t_e}{2} K_{ij}^e \right) \hat{v}_j^m - \frac{3\Delta t_e}{2} \chi (I_{ion})_i^m + \frac{\Delta t_e}{2} \chi (I_{ion})_i^{m-1} + \Delta t_e \chi (I_a)_i^{m+1}. \tag{74}$$

In coupled electro-mechanical simulations the stiffness matrix K_{ij}^e must be recomputed at each time step to account for the changes in the conductivity (35) due to the deformation of the spatial reference frame. This feature represents a form of geometric mechano-electrical feedback [26,54].

The integration of the ionic current by a Galerkin procedure (72) plays a fundamental role in the stability of the presented scheme, since the reaction term is treated explicitly and it represents the coupling term between the PDE and a set of stiff ODEs. The interpolation at the interior of the element is needed for the ionic current integration. Following the State Variable Interpolation (SVI) approach, we define the discrete values of gating variables at the control point location and, successively, they are interpolated at the generic quadrature points θ_{gp} to get the integral (72):

$$\{i_{ion}(v, G_k)\}_{\theta^1=\theta_{gp}} = i_{ion} \left(\sum_{j=1}^{n_s} N_j(\theta_{gp}) \hat{v}_j, \sum_{i=1}^{n_s} N_j(\theta_{gp}) \hat{G}_{k,j} \right). \tag{75}$$

Comparison of different ionic current interpolation strategies within an Isogeometric framework can be found in [54,82].

The system (74) is solved by a simple LU decomposition with partial pivoting. Afterwards, the computed value of transmembrane potential \hat{v}^{n+1} is used to solve the gating variable equations (42) at each control point of the spatial discretization by means of an explicit fourth order Runge-Kutta method. Both reaction-diffusion equation and gating variable equations are advanced with the same time-step size.

3.3. Electro-mechanical coupling

As often observed in cardiac simulations, the monodomain model requires a much finer grid than the mechanical sub-problem to handle the sharp front of the electrophysiological pulse. The optimal solution would be a gradient dependent refinement strategy for the electrophysiological discretization. However, this certainly requires a sophisticated computational framework. The NURBS discretization allows for an efficient implementation of two nested meshes. Indeed, the knot insertion algorithm preserves the geometry and the parametrization, enabling an information exchange by means of simple field evaluations at the Gauss point coordinates. For instance, the displacements are computed at the Gauss points of the electrophysiological mesh evaluating the basis functions R_i at the prescribed set of coordinates. In fact, since the parametrization is preserved, a point is represented by the same parametric coordinates in both discretizations, avoiding complex projections between grids. Thanks to the linearity of Eqs. (66) and (52), such an operation comes at the cost of a matrix-vector multiplication, whose matrix can be computed just once in the pre-analysis stage. The activation function is carried from the electrophysiological mesh to the mechanical discretization and vice-versa for the displacement field. However, in interpolating the field from a univariate to a bivariate domain an additional assumption on the spatial distribution is needed. Specifically, we assume a constant value of the activation function in the θ^2 direction, mimicking the actual muscle activation. In this regard, each problem is tackled with a suitably refined mesh, previously determined by uncoupled convergence analysis.

3.3.1. Space-time convergence of the monodomain model

The minimal time and space scales of the coupled problem are those involved in the propagation of the electrophysiological pulses. Therefore, the sensitivity of the solution to the discretization features needs to be carefully addressed to find out the necessary refinement level. We tested several element and time step sizes against the electrophysiological stimulation of a static axisymmetric emi-ellipsoid corresponding to the subumbrellar surface of the bell. The action potential is triggered by an external current applied in the region within parametric coordinates $0.96 \leq \theta^1 \leq 0.98$ for 1 ms, in order to mimic the activity of the Rhopalpia.

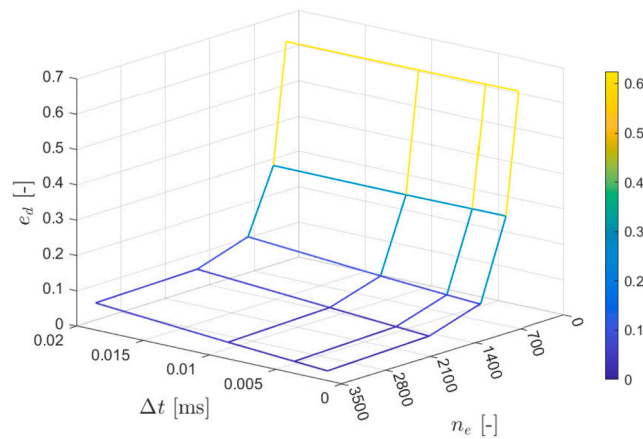


Fig. 5. Convergence of the time-delay error depending on time step size Δt and mesh elements n_e . The colorbar refers to the magnitude of the time-delay error.

Table 1

Summary of the space-time convergence study of the electrophysiological stimulation of the static subumbrellar surface. The APD error is shown as a function of the time step size Δt_e and the element number n_e .

	$\Delta t_e = 0.02$ [ms]	$\Delta t_e = 0.01$ [ms]	$\Delta t_e = 0.005$ [ms]	$\Delta t_e = 0.0025$ [ms]
$n_e = 200$	0.6222	0.6232	0.6240	0.6246
$n_e = 400$	0.2820	0.2808	0.2821	0.2820
$n_e = 800$	0.1025	0.0735	0.0610	0.0554
$n_e = 1600$	0.0553	0.0286	0.0155	0.0092
$n_e = 3200$	0.0491	0.0196	0.0065	-

The domain Ω_e is discretized using quadratic elements, with element numbers $n_e = \{200, 400, 800, 1600, 3200\}$ and time-step sizes $\Delta t_e = \{0.02, 0.01, 0.005, 0.0025\}$ [ms]. We define the error directly using the Action Potential Duration time (APD). The APD is measured as the time interval T_d by which the depolarization front at $v = 0.0$ mV moves from the parametric locations $\theta^1 = 0.2$ to $\theta^1 = 0.8$. Two points aside from the boundaries are considered in order to minimize the influence of boundary conditions on the results. We thus compute the APD time error e_d as:

$$e_d = \frac{T_d - (T_d)_{\text{ref}}}{(T_d)_{\text{ref}}}, \tag{76}$$

assuming the solution from the most refined case $(T_d)_{\text{ref}}$ as reference solution. The error convergence is shown by a combined space-time plot, whereas corresponding data are reported in Table 1. Distinctly, the APD error converges with decreasing time step size and decreasing mesh size and justifies the choice of our reference solution. Different convergence trend are observed in time and space as a consequence of the different theoretical accuracy provided by the discretizations. We observe that with $n_e > 800$ and $\Delta t_e < 0.01$ ms a converged solution can be obtained for the electrophysiological sub-problem.

3.3.2. Calibration of the conductivity coefficient

Most of the Scyphozoans present action potential waves traveling with a conduction velocity in between 45 cm/s and 1 m/s, depending on the species and the specimen maturity [11]. To the best of the author’s knowledge, no conductivity value is available in the literature for the MNN of a Scyphozoan jellyfish. However, several researches report values of conduction velocity of approximately 50.0 cm/s [61,63,48,46]. These data refer to the speed of propagation of the mechanical wave, that is assumed as a proxy for the speed of propagation of the electrical signal. The activation is triggered by the nervous system while the evolution is governed by the muscle properties, resulting in pulses of different duration [60].

In the present work, we seek for a conductivity value that matches a conduction velocity equal to $CV = 47.4$ cm/s, as prescribed in the most recent investigation [46]. To this extent we apply a simple bisection algorithm to the $CV-D_0$ function.

In a generic axisymmetric surface, the wave front is curved, and the CV undergoes spatial variations. To overcome this issue, we conduct the simulations on a cylindrical domain (radius $R = 15.0$ mm and length $L = 20.0$ mm) activated by enforcing the action potential value $v = -69.0$ mV at one end. The resulting wave front propagates in a planar fashion as the radius is constant through the entire domain, indeed. The conduction velocity is measured by the time delay of the wave arrival at two points 4.0 mm and 16.0 mm far from the stimulation site. Although the wave arrival is usually defined using half of the upstroke amplitude, we select time corresponding to $v = +20$ mV to avoid the uncertainties due to the inflection in the depolarization time history (see Fig. 4).

The bisection method employs a fast analysis (600 elements, $p = 2$, $\Delta t = 0.01$ ms) to obtain a preliminary estimation of the conductivity, whereas a more refined discretization (2400 elements, $p = 2$, $\Delta t = 0.0025$ ms) computes an accurate result. The iteration-wise results are summarized in Fig. 6. According to our findings, the conductivity coefficient value corresponding to the target conduction velocity is $D_0 = 1.375e - 05$ nA/(mm mV).

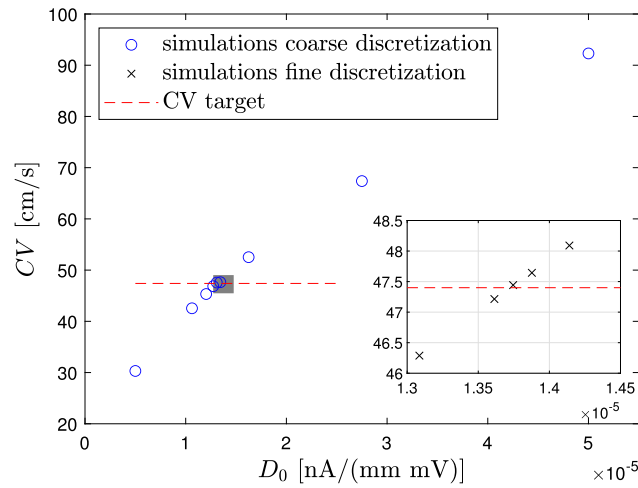


Fig. 6. Tuning of the conductivity coefficient D_0 by a bisection method.

3.4. Finite difference scheme for the fluid problem

The flow field is solved via a centered difference discretization [29]. The moderate computational expense of finite differences allows to use a large number of nodes and to simulate multiple propulsive cycles. The system of equation (47) is solved by means of a fractional step scheme, in the version proposed in [83]. First, a non-solenoidal intermediate velocity field is computed by advancing in time the momentum equation; then, a pressure-correction equation is solved to project the provisional field onto a solenoidal one. The momentum equation is integrated by means of a semi-implicit approach, where the implicit Crank–Nicholson scheme is employed for the viscous terms, and the three-step explicit Runge-Kutta scheme is used for the convective terms. The latter was found to guarantee a good accuracy at moderate CFL (Courant–Friedrichs–Lewy number) values for transitional flow simulations. This yields the discrete momentum equation of the i -th velocity component for the k -th Runge–Kutta substep to be:

$$\frac{\tilde{q}_i - q_i^k}{\Delta t} = -\alpha^k \frac{\partial p^k}{\partial x_i} + \beta^k \mathcal{H}_i^k + \gamma \mathcal{H}_i^{k-1} + \frac{\alpha^k}{2\text{Re}} \mathcal{L}_i (\tilde{q}_i + q_i^k) + f_i^k, \tag{77}$$

where the operators \mathcal{H}_i and \mathcal{L}_i contain the convective terms and the viscous terms, respectively. The time advancement coefficients for three substep levels are $\alpha = [8/15, 2/15, 1/3]$, $\beta = [8/15, 5/12, 3/4]$, $\gamma = [0, -17/60, -5/12]$. The computation of the IB forcing field f_i^k is addressed taking a preliminary fully explicit step for the purpose of interpolating the necessary field variables without further complications in the time scheme, as proposed in [84]. Subsequently, Eq (77) is solved for the increment $\Delta q_i = \tilde{q}_i - q_i^k$:

$$\left(1 - \frac{\Delta t \alpha^k}{2\text{Re}} \mathcal{L}_i\right) \Delta q_i = \left(-\alpha^k \frac{\partial p^k}{\partial x_i} + \beta^k \mathcal{H}_i^k + \gamma \mathcal{H}_i^{k-1} + \frac{\alpha^k}{2\text{Re}} \mathcal{L}_i q_i^k + f_i^k\right) \Delta t \tag{78}$$

The implicit treatment of term in Eq. (78) would the inversion of large sparse matrices. These are reduced to tridiagonal matrices by means of the approximate factorization [85] while introducing a factorization error $\mathcal{O}((\Delta t)^3)$, thus preserving the scheme accuracy in time.

Continuity is enforced by means of the auxiliary scalar field ϕ , used to project the provisional velocity field \tilde{q}_i onto a divergence free-field. Thus, the final velocity and pressure fields at time $n + 1$ can be evaluated as:

$$q_i^{k+1} = \tilde{q}_i - \alpha^k \Delta t \nabla \phi, \tag{79}$$

$$p^{k+1} = p^k + \phi - \frac{\Delta t \alpha^k}{2\text{Re}} \mathcal{L} \phi. \tag{80}$$

The scalar ϕ is computed by taking the divergence of the previous equation and enforcing mass conservation. A Poisson equation is then obtained, reading:

$$\mathcal{L} \phi = \frac{1}{\alpha^k \Delta t} \frac{\partial q_i}{\partial x_i}. \tag{81}$$

A direct solution of the Poisson problem in (81) is preferred to fulfill the continuity equation without any numerical compromise. However, the computational efficiency of the resolution is enhanced by means of the eigen-decomposition of the discrete operator matrices. This technique, well suited in problems where only the forcing term vary from step to step, allows to solve the system in (81) as a sequence of matrix multiplications and inversion of tridiagonal matrices [86].

The space discretization features follow the traces of the work by Verzicco and Orlandi [70], except that only the radial and the axial

directions are resolved. The discrete analogues of the differential operators are obtained by straightforward second-order accurate centered finite differences. The field variables are located on staggered grids, whose beneficial effects in terms of accuracy are discussed in [70,29].

3.4.1. Solid-fluid coupling

Following the approach proposed in [31], the forcing field is computed over a set of Lagrangian Markers (LM) located at the fluid-solid interface and then transferred back to the Eulerian nodes. The LM are distributed in the parametric space of the NURBS patch while requiring the distance between adjacent markers in the physical space to be comparable with that of the underlying Eulerian nodes. Numerical experiments in [87] suggested that a Lagrangian-to-Eulerian spacing ratio below 0.6 only provides a negligible reduction in flux error through the interface. Such an error is further reduced when considering the forcing iterations inherently obtained with the three steps Runge-Kutta scheme used to advance the fluid solution. As pointed out in [88], the repeated enforcement of the volume force f_i^k at each Lagrangian markers on a static contour leads to an improvement of the accuracy of the no-slip condition.

At the LM location the i -th forcing component F_i is evaluated as a body force, by the difference between the current LM velocity v_i and the interpolated velocity value Q_i :

$$F_i(\mathbf{r}_{LM}) = \frac{v_i - Q_i(\mathbf{r}_{LM})}{\Delta t} \tag{82}$$

The interpolation procedure is performed with a Moving Least Squares approach which provides a smooth forcing field even with moving boundaries with minimal smoothing of the interface, especially when exponential weight functions are used [32,33]. The interpolated i -th velocity at the marker location is thus computed by means of the transfer function φ :

$$Q_i(\mathbf{r}_{LM}) = \sum_{j=1}^{N_e} \varphi_j(\mathbf{r}_{LM}) (q_i)_j, \tag{83}$$

where N_e is the number of Eulerian nodes within a local support domain identified for the interpolation procedure. Time indices have been dropped for simplicity of notation. In two-dimensional axisymmetric simulations a 9 points support domain is employed. The same transfer function is used in the spreading of the volume forces (82), but including the scaling factor c_l that accounts for the discrete momentum conservation fulfillment. The volume force at the k -th Eulerian point location is thus evaluated as:

$$f_i^k = \sum_{l=1}^{N_l} c_l \varphi_l^k (F_i)_l, \tag{84}$$

where N_l indicates the number of Lagrangian points associated with the Eulerian point k . A detailed discussion about the properties of the transfer function φ_j and its application within IB methods for viscous flow simulations can be found in [89,32]. It is worth pointing out that when considering $q_1 = rv_1$ no differences occur in the MLS interpolation operators between plane 2D fields and 2D axisymmetric fields.

With the present IB treatment, the flow field across the surface presents a smooth transition layer whose thickness takes at most two Eulerian cells, as shown in [33] with 2D numerical experiments. Therefore, viscous and pressure loads contributing to the external body load F_i^{ext} in equation (56) are evaluated following the procedure thoroughly described in [32,87]. The field variables are interpolated at a probe created along the outward-pointing normal from the surface and transported at the quadrature point laying on the surface by a simplified boundary layer equation. The probe length is selected as the averaged Eulerian cell size.

3.5. Multiphysics solution algorithm

The computation of the action potential at the n -th time step requires the knowledge of the body configuration, whereas the solution of the elastic problem needs the action potential at the same time step. The prediction of the flow field and of the hydrodynamic loads at the n -th time step likewise requires the knowledge of the motion of the body and vice versa. The adopted time-advancement algorithm consists of a sequential approach, where each sub-problem is solved in a segregated fashion and data are progressively transferred as depicted in Fig. 7. Once the monodomain model is solved, the resulting transmbrane potential field $v(\mathbf{r}, t)$ is used to compute the active strain tensor F_a at the quadrature points. The former, together with the hydrodynamic loads computed in the previous fluid step, are set as input field for the elastic analysis. Once obtained the deformed configuration, the immersed boundary procedure allows to enforce the no-slip condition at the fluid-solid interface, and thus to advance the flow field in time.

The comparison of the characteristic time scale of each sub-problem allows to build a computationally affordable time-advancement method. The action potential is expected to exhibit a conduction velocity of about 50 cm/s (see paragraph 3.3.2), whereas the characteristic velocity scale of the fluid-elastic problem can be identified by the product of the neuronal pacing frequency ϕ and the bell diameter $2a_{ex}$. When considering the reference values $\phi = 0.5 \text{ s}^{-1}$ and $2a_{ex} = 3 \text{ cm}$, it yields 1.5 cm/s. In this connection, the time-step size of the simulation is dictated by the electrophysiological sub-problem. Furthermore, the latter suffers from strict stability requirements since the action potential represented in Fig. 4 needs the solution of a 40 ms duration wave front. We therefore employ a sub-stepping technique where the mechanical and fluid-dynamic configurations are updated every M electrophysiological time steps. In the baseline jellyfish simulation presented in section 4 we set $M = 100$, with $\Delta t_e \phi = 2.5 \times 10^{-6}$ and $\Delta t \phi = 2.5 \times 10^{-4}$, since the activation function is observed to exhibit less than 1% overall variation over this time window.

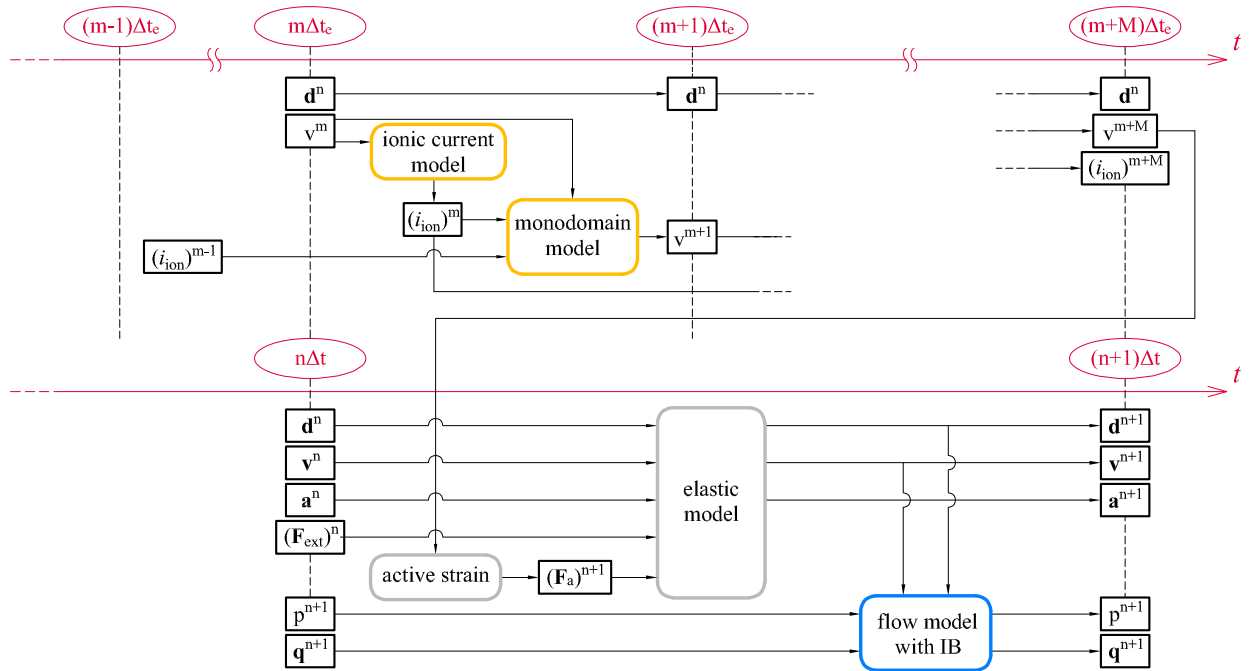


Fig. 7. Sketch of the partitioned, nested numerical scheme with transfer of the fundamental variables among the sub-models. The contour color of each solver corresponds to the color of the sub-domain in the sketches in Fig. 1.

We further simplify the fluid-structure problem by choosing the density of the solid body equal to $\rho_s = 1100 \text{ kg/m}^3$. This is a precaution needed for the sequential fluid-structure algorithm to handle a low solid-to-fluid density ratio without incurring in inaccurate results [90], although the high percentage of body water of real jellyfish entails that $\rho_s = 1000 \text{ kg/m}^3$ would be a more realistic choice. However, the numerical experiments proposed in [91] suggest that such a variation does not significantly affect the swimming kinematics.

4. Fully coupled jellyfish simulations

4.1. Comparison with in-vivo measurements

The complexity of the computational framework and the uncertainty of the bio-mechanical parameters involved in the model gives rise to the need for a comparison with the available in-vivo measurements from a rowing jellyfish. We herein present a qualitative comparison with the kinematics of a 3 cm Aurelia Aurita [7]. The full geometrical and fluid-dynamic similarity is realized in view of replicating the stroke cycle and the resulting swimming features. The model parameters are collected in Table B.3. Following the reference measurements [7], the muscle stretch parameters are tuned such that a relative reduction in the reference diameter $2a_{ex}$ equal to 0.32 is achieved at the peak muscle contraction (the same value is used in [18]). Specifically, we use $a_1 = 0$, $a_3 = 0.096$. The swimming simulations is initialized by applying a 0.1 nA/mm^3 current for 0.1 ms on the still jellyfish body immersed in a quiet fluid. The stimulation is applied within a narrow 0.4 mm subset of the electrophysiological domain at the marginal flap hanging. We employ a rectangular fluid domain of extension $[0, 10a_{ex}]e_1 \otimes [0, 26a_{ex}]e_2$ with homogeneous no-slip boundary conditions expect the symmetry axis. The domain size is chosen such that boundary conditions could have negligible influence on the region where flow gradients develops. The Cartesian grid is uniformly refined only in the subset $[0, 2.4a_{ex}]e_1 \otimes [5, 22a_{ex}]e_2$ with local grid size $\Delta = a_{ex}/250$, whereas a significant grid stretching is implemented in the far-field region. The Eulerian grid resolution was chosen to get 10 grid point within the marginal flaps of the bell, although less grid points are necessary to accurately capture the vortex dynamics.

The jellyfish is placed in the initial position with the uppermost point of the bell at $y = 10a_{ex}$ and it is allowed to run 10 propulsive cycle, where a periodic advancement velocity is achieved within 6 to 8 strokes. The selected pacing frequency is $\phi = 0.5 \text{ Hz}$. The elastic domain is discretized by 35×6 cubic elements in the θ^1 and θ^2 directions, respectively (see Fig. 3 (b)). Conversely, 34 cubic elements are nested within each elastic element to fulfill the convergence requirement discussed in section 3.3.1 for the electrophysiological solution. The monodomain model is advanced in time with the time step-size $\Delta t_e \phi = 2.5 \times 10^{-6}$, in order to achieve the time-convergence threshold (see Fig. 5). The structural and fluid solutions are updated every 100 electrophysiological time steps, namely by $\Delta t \phi = 2.5 \times 10^{-4}$, as discussed in section 3.5.

The comparison with in-vivo measurements in terms of forward swimming speed and cumulative traveled distance in Fig. 8 exhibits a satisfactory agreement. Both the peak and the post-recovery values (the stage where no body displacement occurs) of forward

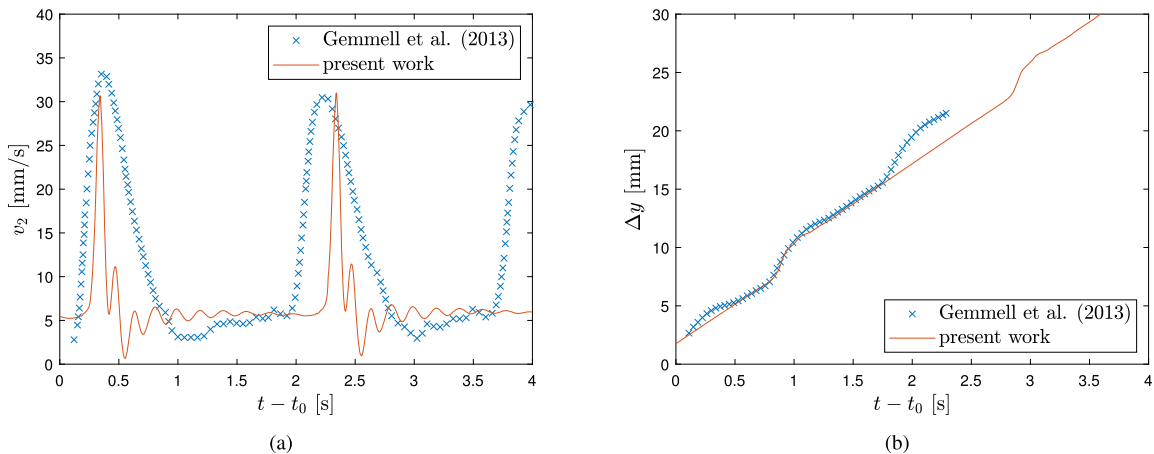


Fig. 8. Comparison with in-vivo measurements on a 3 cm Aurelia Aurita specimen [7]: forward velocity (a), and cumulative traveled distance (b) of the jellyfish center of mass.

velocity are well-reproduced by the model, suggesting that the neuronal activity drives the locomotion with biophysical fidelity at the macroscopic level. High frequency oscillations in the axial velocity are observed in active stress simulation too [77] as the result of the complex interplay between passive elastic properties of the bell and fluid damping. Instantaneous flow fields are displayed in Fig. 9 by vorticity contours. The contraction of the bell margin generates a counter-rotating vortex pair, already observed in oblate species [49], which takes a physiologically relevant role in the swimming process. In the contours of Fig. 9 the starting vortex ring takes negative vorticity values, whereas the stopping vortex ring has a positive vorticity. The former is generated by the roll up of the shear layer occurring with the reduction of the bell marginal section, whereas the latter takes shape from the flow squeezed in between the starting vortex and the bell margin in the recoil stage. The starting vortex travels away from the bell, while the stopping vortex is entrained inside the subumbrellar cavity. The interaction of such vortices with the background fluid motion induced by the bell translation generate a difference in the relative tangential velocity between the inner part and the outer part of the vortex ring. In a laminar flow environment this leads to a pressure gradient acting towards the symmetry axis which squeezes the starting vortex reducing the outer ring diameter. Conversely, the stopping vortex is drawn into the subumbrellar cavity with its core being pushed against the bell wall. In order to quantify the circulation of each vortex, a closed contour line is generated around this vortex with an arbitrary vorticity level, and then the circulation is computed along this line. The shear layers laying in the body proximity are excluded from this computation. The circulation analysis proposed in Fig. 10 confirms that the stopping vortex produces larger circulation values with a delayed peak [7,18] in favor of the propulsion. According to experimental and computational observations [7,77] the clockwise flow rotation inside the bell cavity generates a localized pressure increment that provides the body with additional thrust in the passive motion stage. In the baseline simulation the thrust-enhancement effect of the stopping vortex ring can be detected from the space-time pattern of pressure on the endothelial surface (see the positive pressure stripe in the passive stage in Fig. 11 d). In the second half of the propulsive stage, when the passive advancement occurs, a positive pressure field localized at the central region of the subumbrellar cavity provides additional thrust as a result of the interaction of the stopping vortex ring with the body surface. A similar pattern was observed from pressure contours in Fig. 4 of [7]. This feature leads to enhanced efficiency estimates, since the thrust surplus comes without further muscle contraction.

We further support the discussion about the cruise swimming features of the baseline model by showing in Fig. 11 the space-time pattern of several quantities of interest at the subumbrellar cavity, among which the transmembrane potential v , the activation function γ , the dimensionless radial displacement $u_1/2a_{ex}$, and the pressure p . The active stretching of the muscle fibers takes place after the resting potential value has been retrieved over the full domain, leading to nearly uncoupled dynamics. In the contraction stage the radial displacement closely follows the activation function, whereas in the recovery stage a time gap can be observed between the vanishing of the activation function and the restoration of the undeformed configuration. This means that part of the elastic energy is released after the active strain of the muscle fibers has ended. Such a delicate equilibrium between active contraction and elastic bell features plays a fundamental role in the characterization of the propulsion kinematics. The pressure fluctuations depicted in Fig. 11 (d) result from the oscillations of the bell margin and are related to the swimming speed trend observed in Fig. 8 (a).

4.2. Exploration of the contractility pattern

The thrust generated by oblate jellyfish, as well as the circulation and kinematics of the stopping vortices, was found to be strongly dependent on the radial displacement and velocity of the marginal flaps [18]. These are regulated by the activation pattern of the subumbrellar muscles. We propose a parametric exploration of the neuro-mechanical activation pattern by spanning the parameter space defined by the pair $\{\hat{a}_1, \hat{a}_3\}$. The maximum value of stretching parameters are tuned to match the experimental observations [44] about the cross-area reduction. In this connection, different contractility patterns can be achieved under electrophysiological

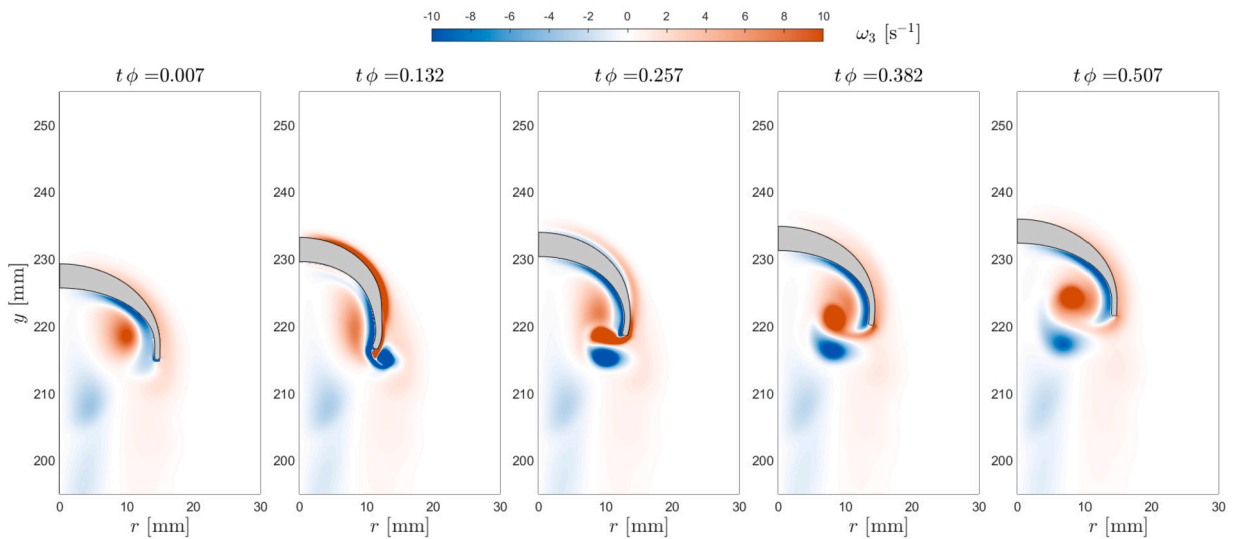


Fig. 9. Instantaneous vorticity contour and body configuration at five subsequent instants of the rowing cycle in the periodic swimming regime. An electrophysiological pacing frequency of $\phi = 0.5$ [Hz] was considered.

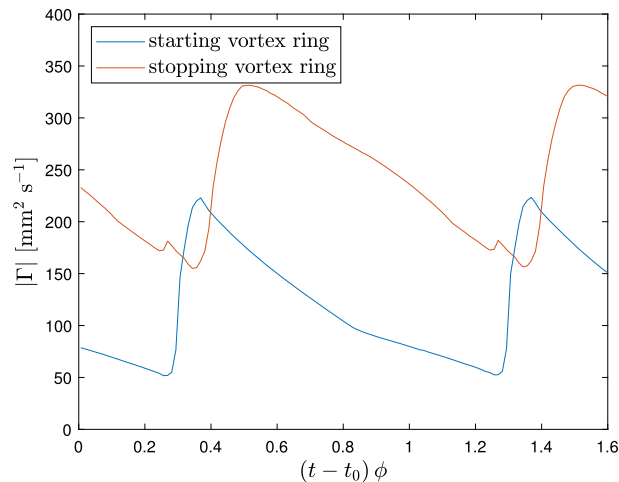


Fig. 10. Time-traces of the circulation modulus, $|\Gamma|$, of the starting and stopping vortex rings within the last propulsive cycle for the baseline case.

stimulation, and the influence of the fibers activation level on the body propulsion can thus be inferred. We point out that a single specimen can exhibit a broad variety of contractility patterns, allowing for equally diverse behaviors. The resulting dynamics is summarized in the phase diagrams in Fig. 12, which depicts the variation of dimensionless mean forward velocity v_2 , kinematic Strouhal number St and strain energy E_s . The notation $\langle \cdot \rangle$ indicates cycle-averaged quantities in the periodic swimming regime. Fig. 12 (a) suggests that the stretching has a different influence on the mean forward velocity concerning coronal and radial fibers. Coronal muscles are responsible for a nearly exponential increase in the swimming speed, whereas radial muscles show a linear dependence. This reflects the relation between local fiber orientation and bell diameter variation; the stretch of coronal fibers directly affects the cross-sectional area of the body, and thus the momentum of expelled fluid, whereas radial fibers enforce the bending of the transverse bell section. Interestingly, the contribution of the radial muscles appear to be more effective for the swimming velocity in the large contraction regime. This suggests that simultaneous activation of both muscle fibers can be a biological resource for escape maneuvers. As postulated in [50,49], the rhopalia might activate the DNN together with the MNN in response to a strong sensory stimulus, driving a simultaneous contraction of radial and coronal fibers. It is acknowledged that some biological functions such as predation and escape can rely on swimming speed rather than minimal metabolic effort [49]. The Strouhal number can further clarify the kinematic picture. Here it is defined as $St = \phi (u_1)_{\max} / \langle v_2 \rangle_c$, following the definition used in [18]. Increasing the amount of coronal stretch, a smaller St is achieved due to the proportionality between subumbrellar volume reduction and advancement velocity. The larger the stretch, the closer the gait to the St stripe of peak efficiency ($St = 0.2 \div 0.4$ [92]), represented by a pink stripe in Fig. 12 (b). Conversely, radial muscles provide a minimal velocity gain compared with the amount of radial displacement they generate. Fig. 12 (c) shows that an increase in \hat{a}_1 does not necessarily bring an increase in the total strain

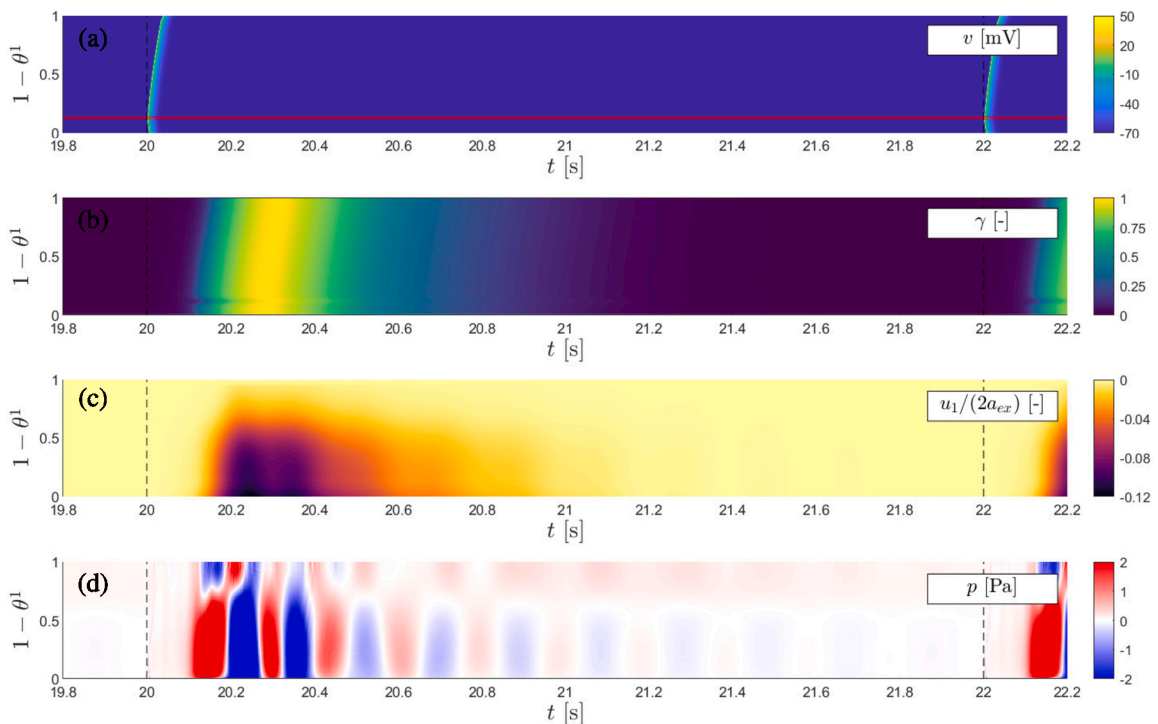


Fig. 11. Space-time pattern of transmembrane potential (a), activation function (b), dimensionless radial displacement (c), and hydrodynamic pressure (d) along the subumbrellar bell profile. Space is represented in convective coordinates at the location $\{1 - \theta^1, 0\}$. Data are taken from the eleventh propulsive cycle of the baseline case where the black dashed lines point out the beginning of the observed cycle. The red lines shows the parametric location where the synaptic stimulation takes place.

energy (comprising the contribution of active and passive deformations), especially at large \hat{a}_3 values. Indeed, activating the radial muscles for enhancing straight swimming might be an energetically and kinematically convenient option.

5. Summary and conclusions

The replication of the neuro-mechanical processes contributing to locomotion can enhance the comprehension of multiple aspects of jellyfish biology and their environmental interactions. At the same time, modern bio-hybrid robotics can benefit from these insights to draw novel engineering solutions which mimic the efficiency and versatility of living species. In this connection we develop a computational framework by which multiphysics aspects of jellyfish straight locomotion can be addressed with the necessary accuracy.

We propose a partitioned method consisting of the sequential solution of three nonlinear coupled sub-problems within an axisymmetric reference frame. In first instance we address the electrophysiological stimulation of the endothelial tissue by means of the monodomain model, which provides the action potential pattern responsible for the muscle contraction. The reaction term relies on the features of a Hodgkin-Huxley type neuron model, specifically tailored for Scyphozoan jellyfish. The electrical activity drives the active contraction of the subumbrellar muscles, which in turn is implemented over a thin layer of the solid domain using the active strain approach. This allows for a straightforward distribution of the fiber contraction in muscle direction according to the biological architecture. Conversely, the passive part of the deformation gradient accounts for the restoration of the undeformed configuration in compliance with the hydrodynamic forces. The active strain method allows to disentangle the effects of radial and coronal muscle orientation on the swimming features of the jellyfish. Both muscle activation parameters and material properties have been tuned to match experimental observations from in-vivo experiments. The overall modeling scenario is extensively described with particular emphasis on the biological background of the modeling choices, and the description is complemented by an extensive validation and verification campaign. Coupling approaches within the multiphysics environment are thoroughly discussed as well. The full model is finally used to successfully replicate the swimming kinematics of a 3-cm *Aurelia Aurita* obtained from in-vivo measurements, and to infer contribution of radial and coronal muscle fibers on the swimming performance. Radial muscle fibers are found to enhance the mean straight swimming speed in the large contractility regime.

The key limitation of the present study lays in the axial symmetry assumption. Although this assumption dramatically reduces the required computational effort, it cuts out some physiological phenomena which might be relevant in the locomotion scenario. Among them we acknowledge the presence of biological appendages, the buckling of the bell margin, already observed in numerical simulations [18], the propagation of three-dimensional excitation waves [46] and the non-simultaneous firing of Rhopalia. The latter was found to be responsible for highly asymmetric muscle contractions which drive turning maneuvers.

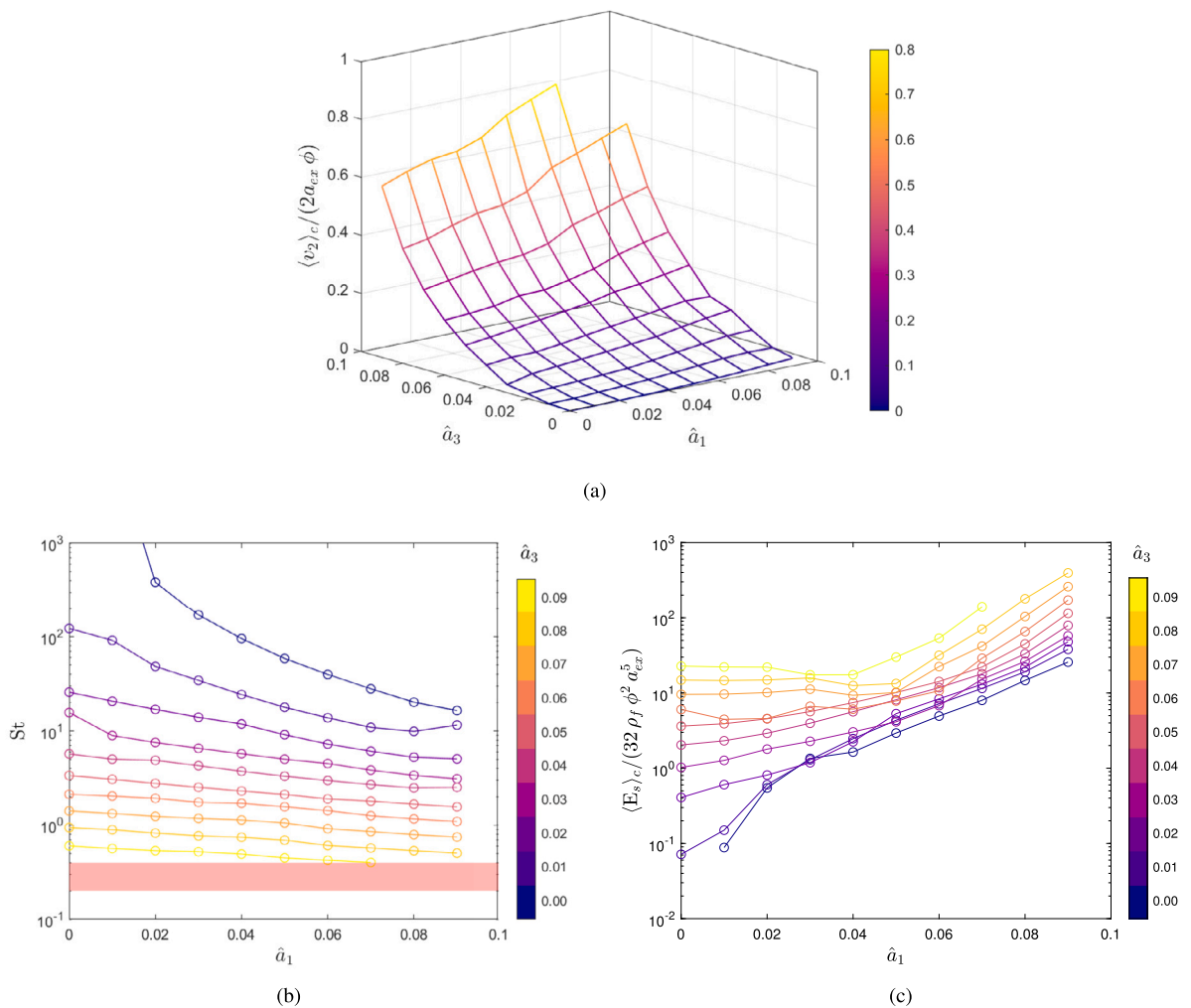


Fig. 12. Diagrams of dimensionless mean forward velocity (a), kinematic Strouhal number (b) and strain energy (c) for different combinations of activation parameters $\{\hat{a}_1, \hat{a}_3\}$. Each curve is associated with a value of \hat{a}_3 , consistently labeled in the adjacent colorbar. The pink stripe in panel (b) encloses the region of peak power efficiency detected by Taylor et al. [92].

The present work will be continued by widening the parameter space exploration to get further physical insights on the jellyfish locomotion. A novel efficiency definition needs to be formulated to account for the active muscle contraction in the propulsion energy scenario. In second instance, the computational tool will be recast for a fully three-dimensional formulation, allowing for the simulation of turning and maneuvering effects.

CRediT authorship contribution statement

Alessandro Nitti: Conceptualization, Methodology, Software, Validation, Visualization, Writing – original draft. **Michele Torre:** Methodology, Software, Validation, Visualization, Writing – original draft. **Alessandro Reali:** Supervision, Writing – review & editing. **Josef Kiendl:** Software, Supervision, Writing – review & editing. **Marco D. de Tullio:** Conceptualization, Software, Supervision, Writing – review & editing.

Declaration of competing interest

The authors declare that they have no known competing interests or personal relationships that could have appeared to influence the work reported in this paper.

Data availability

Data will be made available on request.

Acknowledgements

This work has been partially supported by the Italian Ministry of University and Scientific Research (MIUR) via PRIN2017 XFAST-SIMS Grant No. 20173C478N. A.N. is partially supported by MIUR via “Fondo Sociale Europeo REACT EU—Programma Operativo Nazionale Ricerca e Innovazione 2014–2020”, identifier: C.U.P. D95F21002140006 (D.M. 10/08/2021, n. 1062). D95F21002140006. J.K. has received funding from the European Research Council (ERC) under the European Union’s research and innovation program (grant agreement No. 864482). A.R. and M.T. acknowledge the contribution of the National Recovery and Resilience Plan, Mission 4 Component 2 – Investment 1.4 – CN_00000013 “CENTRO NAZIONALE HPC, BIG DATA E QUANTUM COMPUTING”, spoke 6. A.N. acknowledges Dr. Fabian Pallasdies for the fruitful discussion about the electrophysiological model.

Appendix A. Validation and verification of sub-solvers

In the present section, we provide preliminary verification and validation tests to assess the effectiveness of the implementation in the dedicated reference frame (see Fig. 1) by comparing the simulation output against analytical solutions or experimental and computational data.

A.1. Verification of the electrophysiological solver

The consistency of the discrete solution of the monodomain problem (Eq. (74)) is verified by separately assessing the diffusion and reaction contributions. The diffusion effect is verified by solving the axisymmetric heat equation for the generic scalar field ϕ over a plane circular domain. We consider a disk of radius $R = 40$ m, with Dirichlet boundary conditions $\phi = 1$ prescribed at the domain edge. We assume a thermal diffusivity $k = 60.0$ m²/s. The initial solution consists of $\phi = 0$ all over the inner nodes. Initial solution and boundary conditions entail an axisymmetric diffusion process, where ϕ gradually settles to $\phi = 1.0$ in the whole domain. One should bear in mind that the solution substantially differs from that arising from the diffusion over a cable due to tangential diffusion effects.

The problem is solved up to $t = 2.0$ s over a 1D domain discretized by 600 quadratic elements. A time step size equal to $\Delta t = 0.01$ s is employed. The analytical solution used as reference is obtained by means of the Bessel functions of the first type $J_0(r)$ and its derivative $J_1(r)$, as shown in [93]:

$$\phi(r, t) = 1 - 2 \sum_{n=1}^{\infty} \frac{J_0(\alpha_n r/R)}{\alpha_n J_1(\alpha_n)} \exp(-\alpha_n^2 k t / R^2), \tag{A.1}$$

where α_n is the n -th positive zero of $J_0(r)$. Numerical and analytical solutions are found to coincide at subsequent time steps, as shown in Fig. A.13. Furthermore, the solution is observed to have null gradient at the symmetry axis, testifying the correctness of the implementation.

The reaction effects are validated by integrating the ordinary differential equation associated with the pure neuronal activity, and comparing the time-traces of the action potential with data reported in [25]. Fig. A.13(b) shows that the depolarization phase, as well as the repolarization behavior with the inflection point experimentally observed in [13], match the data available in the literature. Further comparisons have been made for a neuron receiving multiple identical EPSCs with short time-delay, where the depolarization front is observed to interact with the previous repolarization wave.

A.2. Verification of the structural solver

The elastic solver is initially verified against two benchmark problems for which the analytical solution is available. In second instance, the solver is tested against two nonlinear cases undergoing finite displacements and finite strains, and the solutions are compared with those obtained with the commercial software Abaqus [94].

Linear analysis At first, a thick cylindrical tube with constant thickness and an inner pressure load has been simulated. The cylinder has inner and outer radii equal to $R_i = 0.5$ m and $R_o = 1.0$ m, respectively. Axial displacements are constrained on both cylinder ends. For a slender tube, the radial displacement approaches the analytical solution of a thick cylinder with infinite length under internal pressure [95]:

$$u_r(r) = p \frac{R_i^2(1 + \nu)(R_o^2 + r^2(1 - 2\nu))}{E(R_o^2 - R_i^2)r}. \tag{A.2}$$

In the present case the IGA solution was obtained by using: $E = 100$ MPa, $\nu = 0.3$, $p = 0.1$ MPa. Fig. A.14 provides the comparison with the analytical solution. The successful output of this test certifies the effectiveness of the formulation for a configuration with non-unitary, orthogonal local bases.

In second instance, a test-case entailing also non-orthogonal bases is considered. In the field of linear analysis, we simulate a thick hollow sphere subjected to a uniform external pressure. The analytical solution is available from [96] in terms of radial displacement as a function of the radial position:

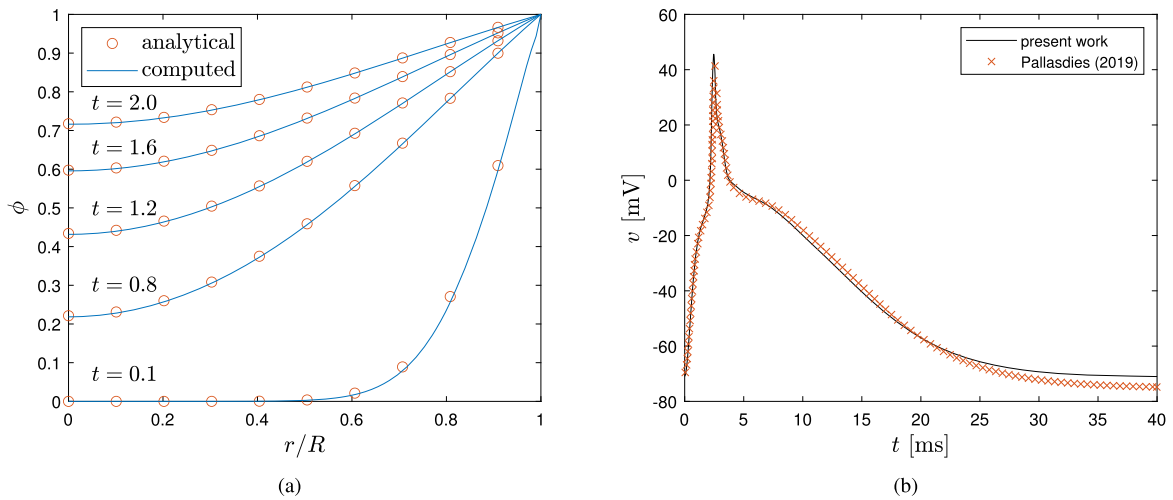


Fig. A.13. Axisymmetric solution of the heat equation over a disk with symmetry-Dirichlet boundary conditions, at subsequent time instants (a). Comparison with the analytical solution (A.1). Time-traces of the transmembrane potential v for a single neuron stimulated by a synaptic EPSC at time zero; comparison with the solution provided in [25] (b).

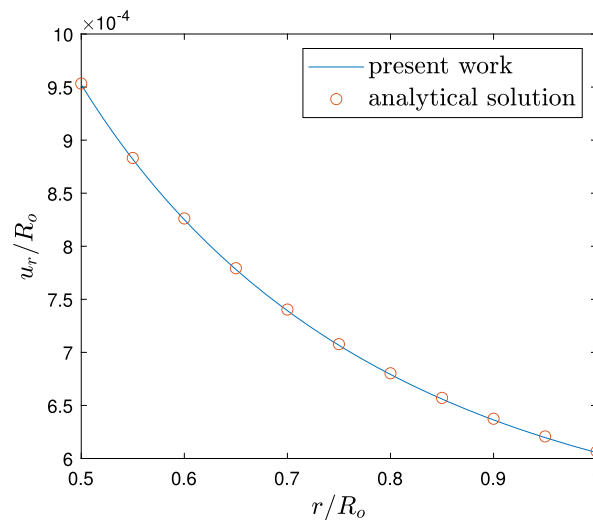


Fig. A.14. Radial displacement as a function of the radial coordinate for a thick cylindrical tube subjected to uniform internal pressure.

$$u_r(r) = r \frac{-pR_o^3}{E(R_o^3 - R_i^3)}(1 - 2\nu) + \frac{1}{r^2} \frac{-pR_i^3 R_o^3}{2E(R_o^3 - R_i^3)}(1 + \nu). \tag{A.3}$$

Our simulation was run with the following parameters: $R_i = 0.5$ m, $R_o = 1.0$ m, $E = 100$ MPa, $\nu = 0.3$, $p = 0.1$ MPa. Unlike the previous test-case, this entails the symmetry axis crossing a solid part of the body. The replication of the analytical solution (see Fig. A.15a) ensures the robustness of the present implementation in presence of quadrature points close to the symmetry axis [34]. One quarter of a circle is simulated, where the tangential displacement is prevented on the equatorial line. The distribution of the radial displacement is checked at different tangential locations. Furthermore, a convergence analyses under h- and p-refinement is performed to check if the integration over the near axis elements degrades the accuracy of the method. The theoretical accuracy is confirmed with quadratic, cubic, and quartic basis functions (see Fig. A.15b).

Nonlinear analysis A cantilever thick tube subjected to internal pressure load is simulated. Boundary and loading conditions are illustrated in the sketch in Fig. A.16a, along with the deformed configuration. For the present test, the compressible Neo-Hookean strain energy function (10) is employed. The chosen physical parameters are: $h = 1.5$ m, $R_i = 0.5$ m, $R_o = 0.8$ m, $p = 0.2$ MPa, $c_{10} = 0.5$ MPa, $K = 1000$ MPa. An accurate IGA solution is achieved with 200 cubic elements, which are able to replicate the Abaqus solution obtained with 4500 CAX8H elements. The numerical solutions have been compared in Fig. A.16b by superposing the radial and axial displacement on the outer profile of the cylinder.

Eventually, the previously described jellyfish geometry was tested with a uniformly distributed radial loading (no displacement-

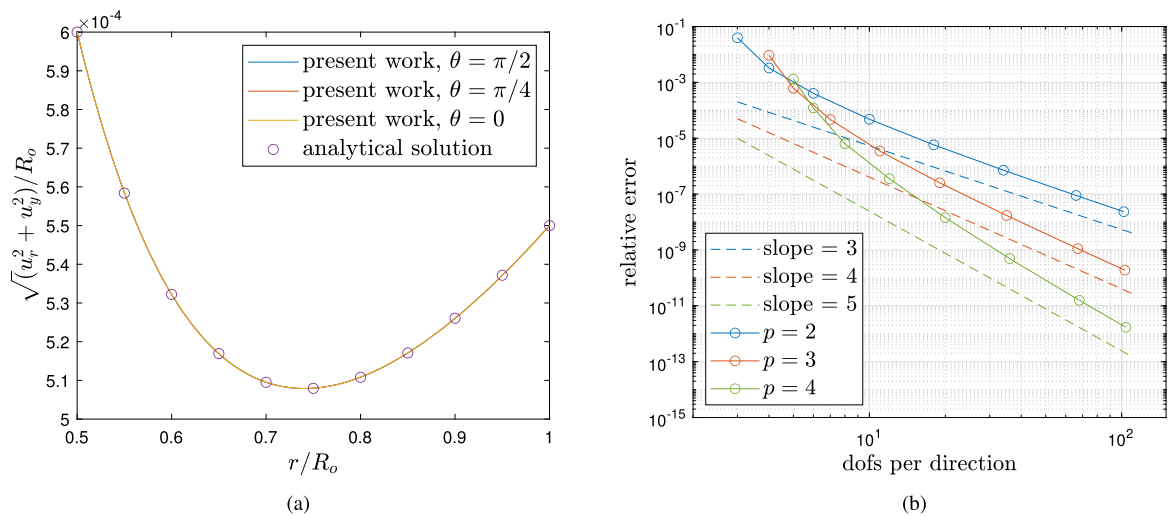


Fig. A.15. Radial displacement of a thick hollow sphere subjected to external pressure as a function of the radial coordinate, for different tangential location (a). Convergence of the error in the local displacement under h-refinement for different basis function orders (b).

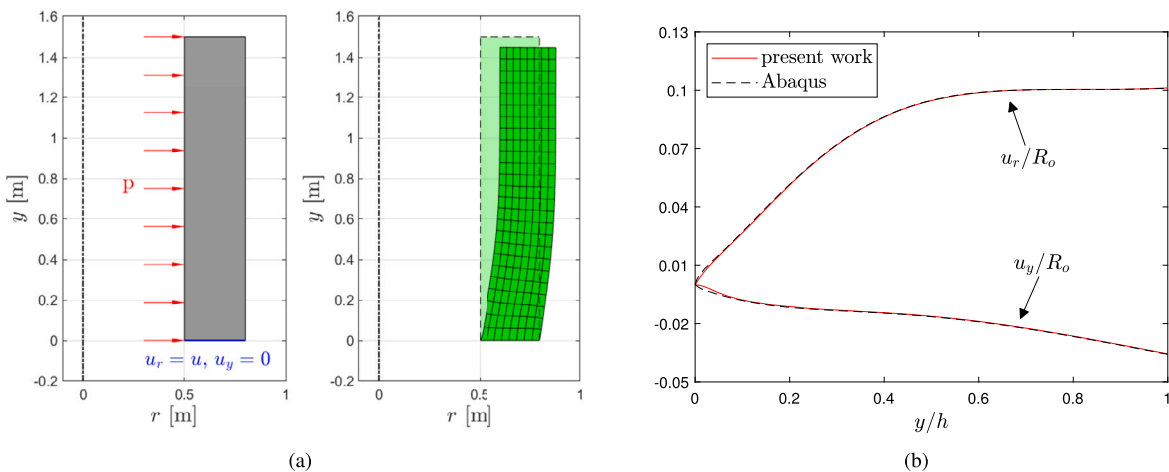


Fig. A.16. Boundary and loading conditions for a cantilever nonlinear cylinder subjected to inner pressure, superposition of reference and deformed configurations (a). Radial and axial displacement as a function of the axial coordinate at the outer cylinder profile (b).

dependent loading) applied on the inner elliptical profile. The force magnitude was calibrated such that the target radial displacement corresponds to a 40% reduction of the cross section area at the bell margin. This represents the largest deformation achieved in our simulation, according to the experimental observations of [73]. In the present test the bell is pinned at the symmetry axis and subjected to a uniformly distributed radial load, obtained by projecting the stress value $p = 2.5$ Pa onto the radial directors over the inner edge. The material law follows Eq. (10), and the material parameters are $c_{10} = 21.67$ Pa, $K = 4.33 \times 10^4$ Pa. The simulation was carried out with 230 cubic elements, and results are compared with those obtained with Abaqus (see Fig. A.17). The Abaqus simulation was run with 13800 CAX4H elements by using the mixed pressure-displacement formulation to alleviate locking effects. With the Abaqus displacement formulation a nearly incompressible material subjected to very large displacement exhibits severe locking effects [97]. The agreement of the IGA solution with the Abaqus output proves that the present implementation with cubic basis functions does not suffer from relevant locking effects, therefore no special treatment is needed. In the present simulation the bulk modulus K yields a volume variations equal to -0.0088%, which nearly fulfills the incompressibility condition. We verified that similar volume variations are obtained when achieving the maximal bell contraction with the active strain approach.

A.3. Verification of the flow solver

Laminar vortex ring formation Vortex rings are fundamental features for the propulsion of oblate species [44]. The simulation of vortex-dominated flows requires the conservation of circulation and kinetic energy to a relatively tight tolerance to ensure that spurious vorticity is not generated. The present scheme, inspired to the work of [70], does preserve these properties in absence of

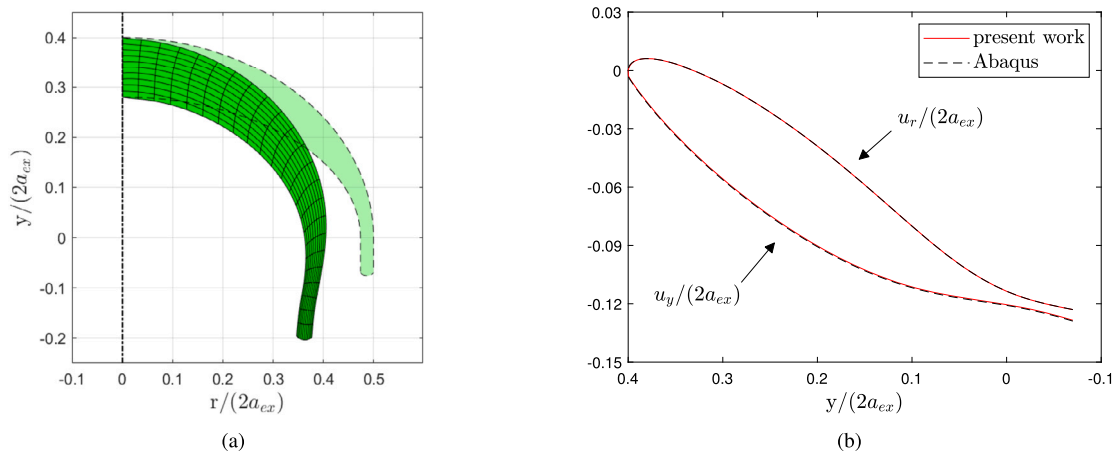


Fig. A.17. Superposition of reference and deformed configurations for a jellyfish model subjected to uniformly distributed horizontal force (a). Radial and axial displacement as a function of the axial coordinate at the outer jellyfish profile (b).

viscosity and time differencing errors. In this regard, simulations of an impulsively started jet are performed to check the formation and evolution of a laminar vortex ring. The test case consists of a cylindrical domain where a coaxial inflow jet impulsively produces a shear layer which evolves into an axisymmetric vortex ring. This actually mimics the jet produced by a piston moving a fluid column through an orifice of diameter D . At time $t = 0$ the flow inside the computational domain is assumed to be at rest. At the inlet the hyperbolic tangent profile is specified:

$$q_2(r, t) = \frac{1}{2} U_p(t) \left[1 - \tanh \left(\frac{2}{\delta_w} \left(\frac{r}{D} - \frac{1}{2} \right) \right) \right], \tag{A.4}$$

where δ_w is the width of the shear layer at the inlet, and $U_p(t)$ provides the time program, defined as:

$$\frac{U_p(t)}{U} = \begin{cases} \frac{1}{2} \left[1 - \cos \left(\pi \frac{t}{t_1} \right) \right], & t \leq t_1 \\ 1.0, & t_1 < t \leq t_2 \\ \frac{1}{2} \left[1 + \cos \left(\pi \frac{t - t_2}{t_1} \right) \right], & t_2 < t \leq t_1 + t_2 \\ 0.0, & t > t_1 + t_2 \end{cases} \tag{A.5}$$

Here, t_1 is the acceleration/deceleration time of the piston, and t_2 represents the stroke ratio. For all cases the piston acceleration was set to $t_1 U m / D = 0.3$ to match the piston motion described in the experiments of [98]. We used a computational domain of extension $[0, 15D] \times [0, 6D]$ with minimal grid size $\Delta y = D/60$ and constant time step size $\Delta t = 0.002U/D$. A free-slip condition is enforced at the outer radial wall, whereas a radiative outflow conditions is employed for the outlet profile. We present two cases for which both computational [99] and experimental [98] data are available. The first is defined by $\delta_w = 0.04$, $t_2 = 6U/D$, $Re = 3100$, whereas the second by: $\delta_w = 0.05$, $t_2 = 8U/D$, $Re = 3100$. The time traces of the dimensionless circulation $\Gamma/(UD)$, plotted in Fig. A.18, reveal full consistency with both experimental and computational data. A qualitative comparison can be carried out by superposing the instantaneous contours of vorticity $\omega = \partial q_2 / \partial r - \partial q_1 / \partial y$ in Fig. A.18(a) with those illustrated in the reference [99].

Steady flow past a torus Subsequently, we simulate the flow past a torus under steady-state conditions. The verification of the simulation output certifies the effectiveness of the IB treatment in the axisymmetric framework. The wake structure behind a torus exhibits different behaviors, depending on several parameters. However, also non-axisymmetric flow fields are observed until the steady-state condition holds [100]. The detached recirculating zone on the axis, the attached recirculating zone, and the detached recirculating zone behind the torus might appear individually or concurrently, depending on the aspect ratio and the Reynolds number [101]. We simulate three different configurations comprising various aspect ratios $AR = D/D_s$ and Reynolds numbers, and compare our results with the numerical outcomes in [101]. Here, D represents the center-line diameter of the torus, whereas D_s is the cross-sectional diameter of the torus. We simulate a torus immersed in a fluid domain of extension $[-15D_s, 25D_s] \times [-AR/2, 20D - AR/2]$, with free-slip conditions on the outer radial wall, and inflow/outflow conditions at the axial edges. A local discretization $\Delta = D/50$ is used in the body-wake region, whereas a cubic grid stretching is employed in the marginal wake regions. Earliest studies showed that the $\{AR, Re\}$ values for the unsteady transition asymptotically approach the values of the straight cylinder, as AR gets larger than 10. For smaller AR values, significantly different wake pattern are observed. We compare the axial velocity profiles for $AR = \{1.3, 2.0, 4.0\}$, at $Re = 70$, with those observed in [101]. The superposition of our data with the profile observed in the reference study (see Fig. A.19) shows acceptable accuracy. The vorticity contours shown in Fig. A.20 illustrate that the location of the stagnation point substantially differs from that of a straight cylinder, corroborating the effectiveness in the representation of axisymmetric flow fields.

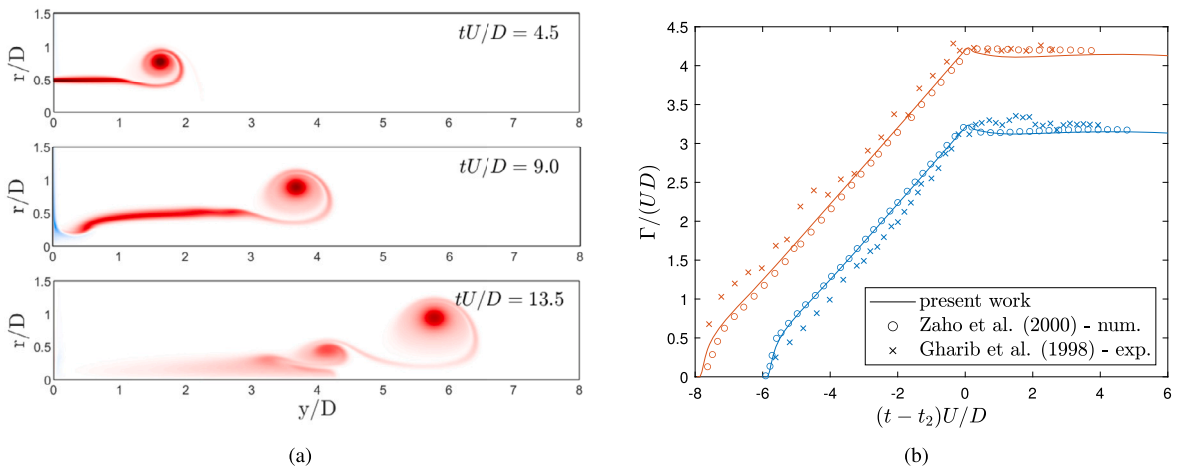


Fig. A.18. Instantaneous vorticity contours showing the detachment of the head vortex ring at three successive time instants for the case $t_2 = 8U/D$ (a). Comparison between present numerical predictions and available measurements for total circulation. Blue refers to the stroke time $t_2 = 6U/D$, whereas orange refers to $t_2 = 8U/D$ (b).

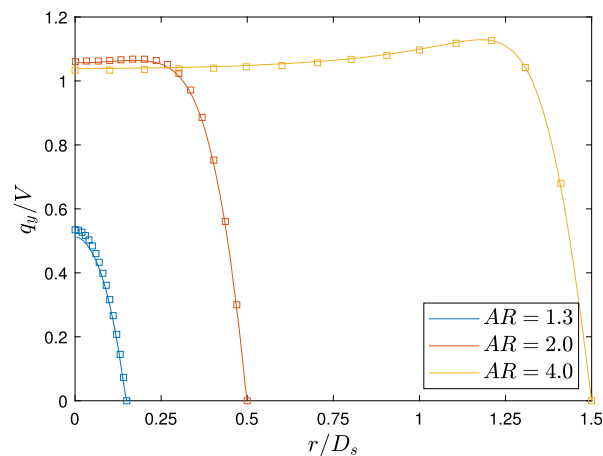


Fig. A.19. Axial velocity profile in correspondence of the torus hole for different aspect ratios. Markers denote the computational results from [101], whereas lines indicate our numerical solution.

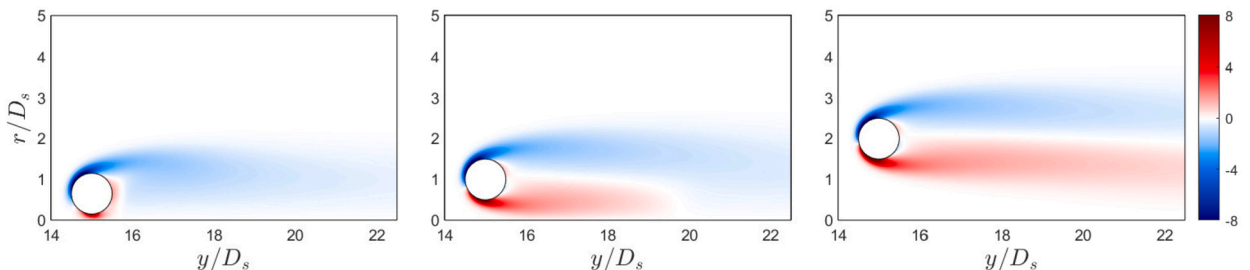


Fig. A.20. Vorticity contours for the flow past a torus at $Re = 70$ with different aspect ratios.

Sphere settling under gravity Eventually, a well-established FSI benchmark test involving axisymmetric flow fields is replicated. The reference work [102] provides an experimental investigation of a sphere settling under gravity in a tank. Measurements carried out by particle image velocimetry, provided the sphere trajectory and velocity, from the moment of its release until rest at the bottom of the tank. The small dimension of the container used in the experiments allows to simulate the flow field under very similar conditions. In the experiments a liquid free surface exists at the top of the domain, whereas we use the no-slip condition at the top of the domain. Several researchers also reproduced the same test with a similar computational setting obtaining a satisfactory agreement with experimental data [103,104]. Half of the sphere is simulated with a local Eulerian resolution of $\Delta = D/50$. The simulation is initialized with the sphere hanging at $8.5D$ from the domain edge and the fluid in a quiescent state. The domain has

Table A.2
Density ratio, settling velocity in infinite medium, Reynolds number and Froude number used in the simulations of a sphere settling under gravity in a closed container.

case	ρ	U_∞	Re	Fr
C1	1.167	0.128	31.9	0.334
C2	1.164	0.091	11.6	0.237
C3	1.161	0.060	4.1	0.156

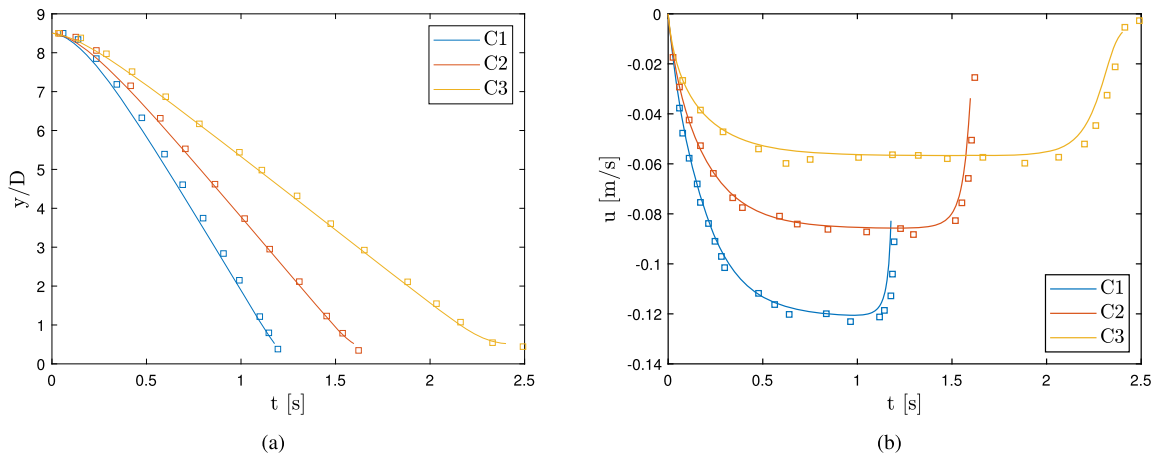


Fig. A.21. Time-traces of position (a) and velocity (b) for a sphere settling under gravity for different phase density ratios. Markers denote the data from [102], whereas lines indicate the numerical solution.

extension $[0, 10.67D] \times [0, -3.33D]$ with no-slip boundary conditions on every boundary, except the symmetry axis. The sphere is allowed to precipitate until it touches the domain boundary. No special treatment is implemented to solve the lubrication layer, but the simulation is stopped when the body approaches the last inner node before the edge. However, the fluid resolution was fine enough to capture the particle deceleration and the formation of an axisymmetric vortex dipole in the wall-approaching phase. The governing parameters of the system are the phase density ratio ρ , and the particle diameter D . We keep the latter constant and run three cases with different ρ values. This inherently leads to different sedimentation velocities and consequently different Reynolds and Froude numbers (parameters listed in Table A.2). The sedimentation trajectory and the sphere velocity are reported in Fig. A.21, where the present results are compared with the experimental data of Ten Cate et al. [102]. A very good agreement is obtained for all the considered configurations.

Appendix B. Summary of physical parameters for the baseline jellyfish model

Table B.3
Summary of physical parameters used for the baseline simulation whose results are presented in section 4.

Description	Symbol	value
Bell outer diameter	$2a_{ex}$	30 [mm]
Bell shear modulus	c_{10}	400 [Pa]
Bell bulk modulus	K	5.0×10^4 [Pa]
Pacing frequency of electrophysiological stimulation	ϕ	0.5 [Hz]
Peak radial muscle stretching	a_1	0 [-]
Peak coronal muscle stretching	a_3	0.096 [-]
Bell density	ρ_s	1100 [kg/m ³]
Active tissue capacitance	C_m	1.0×10^{-3} [mF/mm ²]
Active tissue conductivity	D	1.3745×10^{-5} [nA/(mm mV)]
Current magnitude for stimulation	i_a	0.1 [nA/mm ³]
Duration of applied current for stimulation	-	0.1 [ms]
Fluid density	ρ_f	1000 [kg/m ³]
Fluid viscosity	μ	1.0×10^{-3} [Pa s]
Reynolds number	Re	450 [-]

Appendix C. Supplementary material

Supplementary material related to this article can be found online at <https://doi.org/10.1016/j.apm.2023.08.003>.

References

- [1] J.C. Nawroth, H. Lee, A.W. Feinberg, C.M. Ripplinger, M.L. McCain, A. Grosberg, J.O. Dabiri, K.K. Parker, A tissue-engineered jellyfish with biomimetic propulsion, *Nat. Biotechnol.* 30 (8) (2012) 792–797.
- [2] N.W. Xu, J.P. Townsend, J.H. Costello, S.P. Colin, B.J. Gemmell, J.O. Dabiri, Field testing of biohybrid robotic jellyfish to demonstrate enhanced swimming speeds, *Biomimetics* 5 (4) (2020) 64.
- [3] J. Ye, Y.-C. Yao, J.-Y. Gao, S. Chen, P. Zhang, L. Sheng, J. Liu, LM-Jelly: liquid metal enabled biomimetic robotic jellyfish, *Soft Robot.* 9 (6) (2022) 1098–1107.
- [4] L. Ricotti, B. Trimmer, A.W. Feinberg, R. Raman, K.K. Parker, R. Bashir, M. Sitti, S. Martel, P. Dario, A. Menciassi, Biohybrid actuators for robotics: a review of devices actuated by living cells, *Sci. Robot.* 2 (12) (2017).
- [5] M. Calisti, G. Picardi, C. Laschi, Fundamentals of soft robot locomotion, *J. R. Soc. Interface* 14 (130) (2017) 20170101.
- [6] M. Li, A. Pal, A. Aghakhani, A. Pena-Francesch, M. Sitti, Soft actuators for real-world applications, *Nat. Rev. Mater.* 7 (3) (2022) 235–249.
- [7] B.J. Gemmell, J.H. Costello, S.P. Colin, C.J. Stewart, J.O. Dabiri, D. Tafti, S. Priya, Passive energy recapture in jellyfish contributes to propulsive advantage over other metazoans, *Proc. Natl. Acad. Sci. USA* 110 (44) (2013) 17904–17909.
- [8] M.J. McHenry, Comparative biomechanics: the jellyfish paradox resolved, *Curr. Biol.* 17 (16) (2007) R632–R633.
- [9] R.A. Satterlie, Neuronal control of swimming in jellyfish: a comparative story, *Can. J. Zool.* 80 (10) (2002) 1654–1669.
- [10] A.L. Hodgkin, A.F. Huxley, A quantitative description of membrane current and its application to conduction and excitation in nerve, *J. Physiol.* 117 (4) (1952) 500.
- [11] G.A. Horridge, The nerves and muscles of medusae: V. Double innervation in scyphozoa, *J. Exp. Biol.* 33 (2) (1956) 366–383.
- [12] G.A. Horridge, The nerves and muscles of medusae: VI. The rhythm, *J. Exp. Biol.* 36 (1) (1959) 72–91.
- [13] P.A. Anderson, Ionic currents of the scyphozoa, in: *Evolution of the First Nervous Systems*, Springer, 1989, pp. 267–280.
- [14] J.C. Nawroth, Conceptual Framework and Physical Implementation of a Systematic Design Strategy for Tissue-Engineered Devices, California Institute of Technology, 2013.
- [15] S.P. Colin, J.H. Costello, Morphology, swimming performance and propulsive mode of six co-occurring hydromedusae, *J. Exp. Biol.* 205 (3) (2002) 427–437.
- [16] J.H. Costello, S.P. Colin, J.O. Dabiri, Medusan morphospace: phylogenetic constraints, biomechanical solutions, and ecological consequences, *Invertebr. Biol.* 127 (3) (2008) 265–290.
- [17] S.G. Park, C.B. Chang, W.-X. Huang, H.J. Sung, Simulation of swimming oblate jellyfish with a paddling-based locomotion, *J. Fluid Mech.* 748 (2014) 731–755.
- [18] A.P. Hoover, B.E. Griffith, L.A. Miller, Quantifying performance in the medusan mechanospace with an actively swimming three-dimensional jellyfish model, *J. Fluid Mech.* 813 (2017) 1112–1155.
- [19] J.G. Miles, N.A. Battista, Don't be jelly: exploring effective jellyfish locomotion, arXiv preprint, arXiv:1904.09340, 2019.
- [20] J.O. Dabiri, Landmarks and frontiers in biological fluid dynamics, *Phys. Rev. Fluids* 4 (11) (2019) 110501.
- [21] Z. Lin, A. Hess, Z. Yu, S. Cai, T. Gao, A fluid–structure interaction study of soft robotic swimmer using a fictitious domain/active-strain method, *J. Comput. Phys.* 376 (2019) 1138–1155.
- [22] F. Viola, V. Meschini, R. Verzicco, Fluid–structure-electrophysiology interaction (FSEI) in the left-heart: a multi-way coupled computational model, *Eur. J. Mech. B, Fluids* 79 (2020) 212–232.
- [23] M. Bucelli, A. Zingaro, P.C. Africa, I. Fumagalli, L. Dede, A. Quarteroni, A mathematical model that integrates cardiac electrophysiology, mechanics and fluid dynamics: application to the human left heart, arXiv preprint, arXiv:2208.05551, 2022.
- [24] P.C. Franzone, L.F. Pavarino, S. Scacchi, *Mathematical Cardiac Electrophysiology*, vol. 13, Springer, 2014.
- [25] F. Palladines, S. Goedeke, W. Braun, R.-M. Memmesheimer, From single neurons to behavior in the jellyfish aurelia aurita, *eLife* 8 (2019) e50084.
- [26] F. Nobile, A. Quarteroni, R. Ruiz-Baier, An active strain electromechanical model for cardiac tissue, *Int. J. Numer. Methods Biomed. Eng.* 28 (1) (2012) 52–71.
- [27] T.J. Hughes, J.A. Cottrell, Y. Bazilevs, Isogeometric analysis: Cad, finite elements, nurbs, exact geometry and mesh refinement, *Comput. Methods Appl. Mech. Eng.* 194 (39–41) (2005) 4135–4195.
- [28] A.S. Patelli, L. Dede, T. Lassila, A. Bartzzaghi, A. Quarteroni, Isogeometric approximation of cardiac electrophysiology models on surfaces: an accuracy study with application to the human left atrium, *Comput. Methods Appl. Mech. Eng.* 317 (2017) 248–273.
- [29] P. Orlandi, *Fluid Flow Phenomena: A Numerical Toolkit*, vol. 55, Springer Science & Business Media, 2000.
- [30] P. Moin, R. Verzicco, On the suitability of second-order accurate discretizations for turbulent flow simulations, *Eur. J. Mech. B, Fluids* 55 (2016) 242–245.
- [31] M. Uhlmann, An immersed boundary method with direct forcing for the simulation of particulate flows, *J. Comput. Phys.* 209 (2) (2005) 448–476.
- [32] M. Vanella, E. Balaras, A moving-least-squares reconstruction for embedded-boundary formulations, *J. Comput. Phys.* 228 (18) (2009) 6617–6628.
- [33] M.D. de Tullio, G. Pascasio, A moving-least-squares immersed boundary method for simulating the fluid–structure interaction of elastic bodies with arbitrary thickness, *J. Comput. Phys.* 325 (2016) 201–225.
- [34] O.C. Zienkiewicz, R.L. Taylor, *The Finite Element Method for Solid and Structural Mechanics*, Elsevier, 2005.
- [35] X. Wang, H. Wang, H.R. Brown, Jellyfish gel and its hybrid hydrogels with high mechanical strength, *Soft Matter* 7 (1) (2011) 211–219.
- [36] M.N. Arai, *A Functional Biology of Scyphozoa*, Springer Science & Business Media, 1997.
- [37] W.M. Megill, J.M. Gosline, R.W. Blake, The modulus of elasticity of fibrillin-containing elastic fibres in the mesoglea of the hydromedusa *polyorchis penicillatus*, *J. Exp. Biol.* 208 (20) (2005) 3819–3834.
- [38] K. Joshi, A. Villanueva, C. Smith, D. Murya, J. Blottman, S. Priya, Aurelia aurita inspired artificial mesoglea, *Integr. Ferroelectr.* 148 (1) (2013) 53–66.
- [39] M.E. Demont, J.M. Gosline, Mechanics of jet propulsion in the hydromedusan jellyfish, *polyorchis pexicillatus*: III. A natural resonating bell; the presence and importance of a resonant phenomenon in the locomotor structure, *J. Exp. Biol.* 134 (1) (1988) 347–361.
- [40] A. Lowndes, Percentage of water in jelly-fish, *Nature* 150 (3799) (1942) 234–235.
- [41] S. Hartmann, P. Neff, Polyconvexity of generalized polynomial-type hyperelastic strain energy functions for near-incompressibility, *Int. J. Solids Struct.* 40 (11) (2003) 2767–2791.
- [42] C. Gambini, B. Abou, A. Ponton, A.J. Cornelissen, Micro- and macro-rheology of jellyfish extracellular matrix, *Biophys. J.* 102 (1) (2012) 1–9.
- [43] J. Bonet, R.D. Wood, *Nonlinear Continuum Mechanics for Finite Element Analysis*, Cambridge University Press, 1997.
- [44] J.H. Costello, S.P. Colin, J.O. Dabiri, B.J. Gemmell, K.N. Lucas, K.R. Sutherland, The hydrodynamics of jellyfish swimming, *Annu. Rev. Mar. Sci.* 13 (2020).
- [45] R.A. Satterlie, Control of swimming in the hydrozoan jellyfish *aequorea victoria*: subumbrellar organization and local inhibition, *J. Exp. Biol.* 211 (21) (2008) 3467–3477.
- [46] A.P. Hoover, N.W. Xu, B.J. Gemmell, S.P. Colin, J.H. Costello, J.O. Dabiri, L.A. Miller, Neuromechanical wave resonance in jellyfish swimming, *Proc. Natl. Acad. Sci. USA* 118 (11) (2021).
- [47] L. Passano, Behavioral control systems in medusae; a comparison between hydro- and scyphomedusae, *Publ. Seto Mar. Biol. Lab.* 20 (1973) 615–645.
- [48] L. Passano, Pacemakers and activity patterns in medusae: homage to romanes, *Am. Zool.* 5 (3) (1965) 465–481.

- [49] B.J. Gemmell, S.P. Colin, J.H. Costello, J.O. Dabiri, Suction-based propulsion as a basis for efficient animal swimming, *Nat. Commun.* 6 (1) (2015) 1–8.
- [50] N. Nakanishi, V. Hartenstein, D.K. Jacobs, Development of the rhopalial nervous system in aurelia sp. 1 (cnidaria, scyphozoa), *Dev. Genes Evol.* 219 (6) (2009) 301–317.
- [51] W. Gladfelter, Structure and function of the locomotory system of the scyphomedusa cyanea capillata, *Mar. Biol.* 14 (2) (1972) 150–160.
- [52] C. Cherubini, S. Filippi, P. Nardinocchi, L. Teresi, An electromechanical model of cardiac tissue: constitutive issues and electrophysiological effects, *Prog. Biophys. Mol. Biol.* 97 (2–3) (2008) 562–573.
- [53] D. Ambrosi, G. Arioli, F. Nobile, A. Quarteroni, Electromechanical coupling in cardiac dynamics: the active strain approach, *SIAM J. Appl. Math.* 71 (2) (2011) 605–621.
- [54] A. Nitti, J. Kiendl, A. Gizzi, A. Reali, M.D. de Tullio, A curvilinear isogeometric framework for the electromechanical activation of thin muscular tissues, *Comput. Methods Appl. Mech. Eng.* 382 (2021) 113877.
- [55] D. Ambrosi, S. Pezzuto, Active stress vs. active strain in mechanobiology: constitutive issues, *J. Elast.* 107 (2) (2012) 199–212.
- [56] E.E. Ruppert, R.D. Barnes, R.S. Fox, *Invertebrate Zoology: A Functional Evolutionary Approach*, vol. 592, RUPi, 2004.
- [57] P.A. Anderson, Physiology of a bidirectional, excitatory, chemical synapse, *J. Neurophysiol.* 53 (3) (1985) 821–835.
- [58] J.P. Keener, J. Sneyd, *Mathematical Physiology*, vol. 1, Springer, 1998.
- [59] P.A. Anderson, W.E. Schwab, The organization and structure of nerve and muscle in the jellyfish cyanea capillata (coelenterata; scyphozoa), *J. Morphol.* 170 (3) (1981) 383–399.
- [60] R.A. Satterlie, A.N. Spencer, Neuronal control of locomotion in hydrozoan medusae, *J. Comp. Physiol.* 150 (2) (1983) 195–206.
- [61] G.A. Horridge, et al., The Nerves and Muscles of Medusae. I. Conduction in the Nervous System of Aurelia Aurita Lamarck, 1954.
- [62] A. Spencer, R.A. Satterlie, The action potential and contraction in subumbrellar swimming muscle of polychaete penicillatus (hydromedusae), *J. Comp. Physiol.* 144 (3) (1981) 401–407.
- [63] R.A. Satterlie, Cnidarian nerve nets and neuromuscular efficiency, *Integr. Comp. Biol.* 55 (6) (2015) 1050–1057.
- [64] T. Katsuki, R.J. Greenspan, Jellyfish nervous systems, *Curr. Biol.* 23 (14) (2013) R592–R594.
- [65] E.D. Tytell, C.-Y. Hsu, T.L. Williams, A.H. Cohen, L.J. Fauci, Interactions between internal forces, body stiffness, and fluid environment in a neuromechanical model of lamprey swimming, *Proc. Natl. Acad. Sci. USA* 107 (46) (2010) 19832–19837.
- [66] S. Göktepe, A. Menzel, E. Kuhl, The generalized hill model: a kinematic approach towards active muscle contraction, *J. Mech. Phys. Solids* 72 (2014) 20–39, <https://doi.org/10.1016/j.jmps.2014.07.015>, <https://www.sciencedirect.com/science/article/pii/S0022509614001598>.
- [67] S.A. Niederer, N.P. Smith, The role of the frank–starling law in the transduction of cellular work to whole organ pump function: a computational modeling analysis, *PLoS Comput. Biol.* 5 (4) (2009) e1000371, <https://doi.org/10.1371/journal.pcbi.1000371>.
- [68] S. Niederer, P. Hunter, N. Smith, A quantitative analysis of cardiac myocyte relaxation: a simulation study, *Biophys. J.* 90 (5) (2006) 1697–1722, <https://doi.org/10.1529/biophysj.105.069534>.
- [69] T.L. Daniel, Mechanics and energetics of medusan jet propulsion, *Can. J. Zool.* 61 (6) (1983) 1406–1420.
- [70] R. Verzicco, P. Orlandi, A finite-difference scheme for three-dimensional incompressible flows in cylindrical coordinates, *J. Comput. Phys.* 123 (2) (1996) 402–414.
- [71] S.G. Park, B. Kim, J. Lee, W.-X. Huang, H.J. Sung, Dynamics of prolate jellyfish with a jet-based locomotion, *J. Fluids Struct.* 57 (2015) 331–343.
- [72] J.O. Dabiri, S.P. Colin, J.H. Costello, Morphological diversity of medusan lineages constrained by animal–fluid interactions, *J. Exp. Biol.* 210 (11) (2007) 1868–1873.
- [73] M. Ford, J. Costello, Kinematic comparison of bell contraction by four species of hydromedusae, *Sci. Mar.* 64 (S1) (2000) 47–53.
- [74] J.O. Dabiri, S.P. Colin, J.H. Costello, M. Gharib, Flow patterns generated by oblate medusan jellyfish: field measurements and laboratory analyses, *J. Exp. Biol.* 208 (7) (2005) 1257–1265.
- [75] M. Sahin, K. Mohseni, An arbitrary Lagrangian–Eulerian formulation for the numerical simulation of flow patterns generated by the hydromedusa aequorea victoria, *J. Comput. Phys.* 228 (12) (2009) 4588–4605.
- [76] G. Herschlag, L. Miller, Reynolds number limits for jet propulsion: a numerical study of simplified jellyfish, *J. Theor. Biol.* 285 (1) (2011) 84–95.
- [77] A.P. Hoover, A.J. Porras, L.A. Miller, Pump or coast: the role of resonance and passive energy recapture in medusan swimming performance, *J. Fluid Mech.* 863 (2019) 1031–1061.
- [78] L. Piegel, W. Tiller, *The NURBS Book*, Springer Science & Business Media, 1996.
- [79] J.A. Cottrell, T.J. Hughes, Y. Bazilevs, *Isogeometric Analysis: Toward Integration of CAD and FEA*, John Wiley & Sons, 2009.
- [80] J. Kiendl, M.-C. Hsu, M.C. Wu, A. Reali, Isogeometric Kirchhoff–Love shell formulations for general hyperelastic materials, *Comput. Methods Appl. Mech. Eng.* 291 (2015) 280–303.
- [81] M. Ethier, Y. Bourgault, Semi-implicit time-discretization schemes for the bidomain model, *SIAM J. Numer. Anal.* 46 (5) (2008) 2443–2468.
- [82] M. Torre, S. Morganti, A. Nitti, M.D. de Tullio, F.S. Pasqualini, A. Reali, An efficient isogeometric collocation approach to cardiac electrophysiology, *Comput. Methods Appl. Mech. Eng.* 393 (2022) 114782.
- [83] P. Moin, J. Kim, Numerical investigation of turbulent channel flow, *J. Fluid Mech.* 118 (1982) 341–377.
- [84] J. Kim, D. Kim, H. Choi, An immersed-boundary finite-volume method for simulations of flow in complex geometries, *J. Comput. Phys.* 171 (1) (2001) 132–150.
- [85] J.H. Ferziger, M. Perić, R.L. Street, *Computational Methods for Fluid Dynamics*, vol. 3, Springer, 2002.
- [86] D.B. Haidvogel, T. Zang, The accurate solution of Poisson’s equation by expansion in Chebyshev polynomials, *J. Comput. Phys.* 30 (2) (1979) 167–180.
- [87] A. Nitti, J. Kiendl, A. Reali, M.D. de Tullio, An immersed-boundary/isogeometric method for fluid–structure interaction involving thin shells, *Comput. Methods Appl. Mech. Eng.* 364 (2020) 112977.
- [88] W.-P. Breugem, A second-order accurate immersed boundary method for fully resolved simulations of particle-laden flows, *J. Comput. Phys.* 231 (13) (2012) 4469–4498.
- [89] G.-R. Liu, Y.-T. Gu, *An Introduction to Meshfree Methods and Their Programming*, Springer Science & Business Media, 2005.
- [90] C. Förster, W.A. Wall, E. Ramm, Artificial added mass instabilities in sequential staggered coupling of nonlinear structures and incompressible viscous flows, *Comput. Methods Appl. Mech. Eng.* 196 (7) (2007) 1278–1293.
- [91] W.-X. Huang, H.J. Sung, An immersed boundary method for fluid–flexible structure interaction, *Comput. Methods Appl. Mech. Eng.* 198 (33–36) (2009) 2650–2661.
- [92] G.K. Taylor, R.L. Nudds, A.L. Thomas, Flying and swimming animals cruise at a strouhal number tuned for high power efficiency, *Nature* 425 (6959) (2003) 707–711.
- [93] E.W. Weisstein, *Heat conduction equation—disk*, <https://mathworld.wolfram.com/HeatConductionEquationDisk.html>, 2022.
- [94] M. Smith, *ABAQUS/Standard User’s Manual*, Version 6.9, Dassault Systèmes Simulia Corp., United States, 2009.
- [95] S.P. Timoshenko, J.N. Goodier, *Theory of Elasticity*, McGraw-Hill, 1951.
- [96] M. Kholdi, A. Loghman, H. Ashrafi, M. Arefi, Analysis of thick-walled spherical shells subjected to external pressure: elastoplastic and residual stress analysis, *Proc. Inst. Mech. Eng. Part L, J. Mater.: Des. Appl.* 234 (1) (2020) 186–197.
- [97] T.J. Hughes, *The Finite Element Method: Linear Static and Dynamic Finite Element Analysis*, Courier Corporation, 2012.
- [98] M. Gharib, E. Rambod, K. Shariff, A universal time scale for vortex ring formation, *J. Fluid Mech.* 360 (1998) 121–140.
- [99] W. Zhao, S.H. Frankel, L.G. Mongeau, Effects of trailing jet instability on vortex ring formation, *Phys. Fluids* 12 (3) (2000) 589–596.

- [100] G.J. Sheard, K. Hourigan, M.C. Thompson, Computations of the drag coefficients for low-Reynolds-number flow past rings, *J. Fluid Mech.* 526 (2005) 257–275.
- [101] P. Yu, Steady flow past a torus with aspect ratio less than 5, *J. Fluids Struct.* 48 (2014) 393–406.
- [102] A. Ten Cate, C. Nieuwstad, J. Derksen, H. Van den Akker, Particle imaging velocimetry experiments and lattice-Boltzmann simulations on a single sphere settling under gravity, *Phys. Fluids* 14 (11) (2002) 4012–4025.
- [103] T. Kempe, J. Fröhlich, An improved immersed boundary method with direct forcing for the simulation of particle laden flows, *J. Comput. Phys.* 231 (9) (2012) 3663–3684.
- [104] C.-C. Liao, Y.-W. Chang, C.-A. Lin, J. McDonough, Simulating flows with moving rigid boundary using immersed-boundary method, *Comput. Fluids* 39 (1) (2010) 152–167.